J. Fluid Mech. (2006), *vol.* 548, *pp.* 207–235.
doi:10.1017/S0022112005007627 Printed in the United Kingdom

Stability of axisymmetric core–annular flow in the presence of an insoluble surfactant

By M. G. BLYTH[1], H. LUO[2] AND C. POZRIKIDIS[2]

[1]School of Mathematics, University of East Anglia, Norwich, NR4 7TJ, UK

[2]Department of Mechanical and Aerospace Engineering, University of California, San Diego, La Jolla, CA 92093-0411, USA

(Received 31 January 2003 and in revised form 14 July 2005)

The effect of an insoluble surfactant on the stability of the core–annular flow of two immiscible fluids is investigated by a normal-mode linear analysis and by numerical simulations based on the immersed-interface method for axisymmetric perturbations. The results reveal that, although the Marangoni stress due to surfactant concentration variations is unable to initiate a new type of instability as in the case of two-dimensional two-layer channel flow, it does destabilize the interface by broadening the range of growing wavenumbers and by raising the growth rate of unstable perturbations. Numerical simulations for large-amplitude disturbances reveal that the surfactant plays an important role in determining the morphology of the interfacial structures developing in the nonlinear stages of the motion.

1. Introduction

The stability of the core–annular flow has been discussed extensively in the literature with reference to lubricated pipeline transport, two-phase flow in porous media, and flow in the airways of the lung, as reviewed by Joseph & Renardy (1993), Joseph *et al.* (1997), and Renardy (1997), and more recently by Kouris & Tsamopoulos (2001, 2002), Wei & Rumschitzki (2002*a*, *b*), and Grotberg & Jensen (2004). In the absence of flow, the core–annular arrangement falls prey to the Rayleigh capillary instability leading to the deposition of the outer fluid into annular lobes attached to the wall in the case of thin annular layers, or to dispersion of a series of drops separated by lenticular bridges that occlude the tube cross-section in the case of thicker annular layers. Normal-mode stability analysis and numerical simulations of the core–annular flow have demonstrated that the shearing action of the basic flow has a stabilizing influence at sufficiently high Reynolds numbers (e.g. Russo & Steen 1989; Georgiou *et al.* 1992; Kouris & Tsamopoulos 2001, 2002). When instability occurs, the cylindrical interface develops axisymmetric bamboo and sawtooth waves or three-dimensional corkscrew and snake waves. Unsaturated growth leads to breakup of the core fluid into drops and slugs and may cause a transition to an altered state in which the fluids are stratified.

Several authors have studied the effect of an insoluble surfactant on the instability of a stationary arrangement and noted that the surfactant may reduce the growth rate of disturbances by as much as a quarter (e.g. Carroll & Lucassen 1974; Otis *et al.* 1993; Cassidy *et al.* 1999). Kwak & Pozrikidis (2001) confirmed that the growth rate of the capillary instability non-dimensionalized by the unperturbed surface tension is reduced owing to the Marangoni interfacial tractions associated with variations

in the surfactant concentration. However, in the presence of a mean flow, the time scale of the instability should be defined by the mean, centreline, or interfacial velocity, and the rescaling necessitates a re-interpretation of the earlier work. The possibly destabilizing effect of the surfactant under the new non-dimensionalization is in contrast with conventional wisdom, which anticipates that adding a surfactant will reduce the surface tension and thereby slow down the growth of the capillary instability. To reconcile these viewpoints, we observe that the base-state surface tension instead of the clean-interface surface tension is used to perform the necessary non-dimensionalizations.

Consideration of the effect of the surfactant on the core–annular flow is partly motivated by the discovery that an insoluble surfactant may promote or initiate the growth of interfacial waves in two-dimensional two-layer channel flow, even under conditions of Stokes flow (Frenkel & Halpern 2002; Halpern & Frenkel 2003; Blyth & Pozrikidis 2004*a*, *b*, *c*; Pozrikidis 2004*a*, *b*). Conversely, a shear flow may destabilize an otherwise stable interface populated by surfactants owing to the growth of the so-called Marangoni mode, which is complementary to the Yih mode due to viscosity stratification. Although these results are highly suggestive of the destabilizing influence of the surfactant in core–annular flow, it is possible that the effect may be masked by the Rayleigh–Tomotika capillary instability of the cylindrical interface in the axisymmetric configuration. On the other hand, because the capillary instability is intermittently suppressed at sufficiently high mean-flow velocities, the Marangoni mode may dominate the stable regimes of the uncontaminated flow.

Kas-Danouche, Papageorgiou & Siegel (2004) performed an asymptotic analysis of the instability of the core–annular flow in the presence of an insoluble surfactant, in the limit where the annulus is thin compared to the core and the wave period is of the order of the tube radius. The mathematical model results in a system of two coupled nonlinear partial differential equations for the interfacial amplitude and the surface surfactant concentration. Solving these equations to assess the precise effect of the surfactant was left as a topic for further work. Wei (2005) and Wei & Rumschitzki (2005) demonstrated that, when the annular layer is much thinner than the core, the surfactant extends the range of unstable wavenumbers. An analysis for a time-periodic base flow has been performed by Wei, Halpern & Grotberg (2005).

In this work, we study the stability of the core–annular flow in the presence of an insoluble surfactant by undertaking a normal-mode linear stability analysis and also by performing complementary numerical simulations of the large-amplitude motion using a finite-difference method combined with Peskin's immersed-interface approach (e.g. Peskin 2002). Previous authors have performed simulations of the axisymmetric flow in the absence of surfactant in straight and periodically constricted tubes using the volume-of-fluid (VOF) method (Li & Renardy 1999), and spectral expansions coupled with domain mapping (Kouris & Tsamopoulos 2001, 2002). In both parts of the present study, axisymmetric disturbances are also considered. However, the severity of this restriction is ameliorated by the discovery that axisymmetric modes are known to be most dangerous for a clean interface (Preziosi, Chen & Joseph 1989). The numerical results will show that the primary destabilizing effect of the surfactant is to extend the range of unstable linear modes to a wider range of wavenumbers. Although the nonlinear features of the instability are generally similar to those observed in clean fluids, with wave overturning and the formation of slugs and drops occurring under certain conditions, it will be shown that the surfactant is responsible for a much richer dynamics.

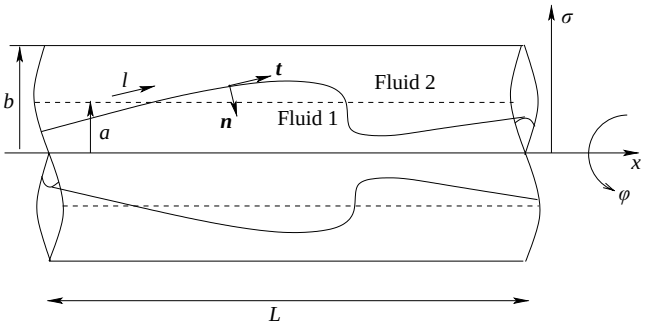

FIGURE 1. Schematic illustration of axisymmetric core–annular flow in a circular tube.

2. Problem statement

We consider the axisymmetric, pressure-driven core–annular flow of two immiscible Newtonian fluids in a circular cylinder of radius b, and introduce cylindrical polar coordinates, (x, σ, φ), as illustrated in figure 1. All geometrical and flow variables are assumed to be independent of the azimuthal angle, φ. The inner and outer fluids are labelled, respectively, by the subscripts 1 and 2. The interface is occupied by an insoluble surfactant with surface concentration Γ, that is convected and diffuses over the interface to alter the local surface tension, γ, according to an assumed surface equation of state.

When the surface surfactant concentration is well below the saturation level, a linear relationship may be assumed between the surface tension and the surfactant concentration according to Gibbs' law, $\gamma_c - \gamma = \Gamma E$, where E is the surface elasticity and γ_c is the surface tension of a clean interface which is devoid of surfactants (e.g. Pozrikidis 2004*a*). In terms of the dimensionless physiochemical parameter $\beta = \Gamma_0 E/\gamma_c$, the linear equation of state reads

$$\gamma = \frac{\gamma_0}{1-\beta}\left(1 - \beta\frac{\Gamma}{\Gamma_0}\right), \tag{2.1}$$

where Γ_0 is a reference concentration corresponding to the surface tension $\gamma_0 = \gamma_c(1-\beta)$. The significance of the surfactant is expressed by the dimensionless Marangoni number,

$$Ma \equiv \frac{E\Gamma_0}{\gamma_0} = \frac{\beta}{1-\beta}. \tag{2.2}$$

Nonlinear equations of state incorporating non-ideal surfactant behaviour and surface saturation are reviewed by Pozrikidis (2004*a*).

The individual fluid motions in the core and annulus are governed by the Navier–Stokes and the continuity equation, subject to the no-slip and no-penetration conditions at the tube wall, the usual kinematic condition requiring continuity of velocity at the interface, and a dynamic condition expressing a balance between the hydrodynamic traction exerted on either side of the interface, surface tension and Marangoni traction due to the surfactant. Specifically, the dynamic condition requires

$$\Delta \boldsymbol{f} \equiv \left(\boldsymbol{\sigma}^{(1)} - \boldsymbol{\sigma}^{(2)}\right)\cdot\boldsymbol{n} = \gamma\, 2\kappa_m\, \boldsymbol{n} - \frac{\partial\gamma}{\partial l}\,\boldsymbol{t}, \tag{2.3}$$

where $\boldsymbol{\sigma}^{(j)}$ is the Newtonian stress tensor in the jth fluid, $\boldsymbol{n}$ is the unit normal vector pointing into the core fluid, $\boldsymbol{t}$ is the unit tangent vector pointing in the direction of

increasing arclength l, and $\kappa_m = (1/2)\,\nabla\cdot\boldsymbol{n}$ is the mean curvature of the axisymmetric interface, as illustrated in figure 1.

In the axisymmetric configuration, the surfactant surface concentration, $\Gamma(x,t)$, evolves according to the convection–diffusion equation

$$\frac{\mathrm{d}\Gamma}{\mathrm{d}t} = w\,\frac{\partial\Gamma}{\partial l} - \frac{1}{\sigma}\frac{\partial(\sigma u_t \Gamma)}{\partial l} - \Gamma\, 2\kappa_m\, u_n + \frac{D_s}{\sigma}\frac{\partial}{\partial l}\left(\sigma\frac{\partial\Gamma}{\partial l}\right), \tag{2.4}$$

where $u_t = \boldsymbol{u}\cdot\boldsymbol{t}$ and $u_n = \boldsymbol{u}\cdot\boldsymbol{n}$ are the interfacial velocities in the directions of the tangential and normal vectors along the contour of the interface in an azimuthal plane, and D_s is the surface surfactant diffusivity (Li & Pozrikidis 1997; Yon & Pozrikidis 1998). The derivative $\mathrm{d}/\mathrm{d}t$ on the left-hand side of (2.4) denotes the rate of change of a variable following the motion of the interfacial marker points moving with the component of the fluid velocity normal to the interface, and with an arbitrary tangent velocity, $w(l)$. If $w=0$, the nodes reduce to marker points moving normal to the interface; if $w=u_t$, the nodes are Lagrangian point particles moving with the local fluid velocity.

When the interface is perfectly cylindrical and the surfactant concentration is uniform and equal to Γ_0, both the velocity and the shear stress are continuous across the interface, and the flow is unidirectional. A cylindrical interface can be established if the pipe is vertical, or else if the fluid densities are perfectly or nearly matched so that the effect of gravity is insignificant. For simplicity, we consider fluids with equal densities, where gravity plays no role. The piecewise parabolic velocity profile of the basic flow is given by

$$\left.\begin{aligned} u_x &= \frac{\chi}{4\mu_1}(a^2-\sigma^2) + u_I \quad \text{for } 0\leqslant\sigma\leqslant a,\\ u_x &= -\frac{\chi}{4\mu_2}(\sigma^2-a^2) + u_I \quad \text{for } a\leqslant\sigma\leqslant b, \end{aligned}\right\} \tag{2.5}$$

where a is the interface radius, χ is the negative of the streamwise pressure gradient, μ_1 and μ_2 are the viscosity of the core and annular fluid, and u_I is interfacial velocity given by

$$u_I = \frac{\chi}{4\mu_2}(b^2-a^2), \tag{2.6}$$

independent of the viscosity of the core fluid. The corresponding pressure distribution is given by

$$p_1^{(0)}(x,\sigma) = -\chi x + P_0, \qquad p_2^{(0)}(x,\sigma) = -\chi x - \frac{\gamma_0}{a} + P_0, \tag{2.7}$$

for $j=1,2$, where γ_0 is the unperturbed surface tension corresponding to the surfactant concentration Γ_0, and P_0 is an indeterminate constant.

To examine the effect of the surfactant on the stability of the basic unidirectional flow subject to axisymmetric perturbations, we first perform a normal-mode linear stability analysis for Navier–Stokes and Stokes flow, and then carry out numerical simulations of the nonlinear motion using a finite-difference method combined with Peskin's immersed-interface approach.

3. Formulation of the linear stability problem

In the presence of a minor axisymmetric disturbance, the cylindrical interface is displaced to a new position described by

$$\sigma = f(x,t) = a + \varepsilon\eta(x,t), \tag{3.1}$$

where ε is a small dimensionless number, and η is the wave form of the perturbation. Correspondingly, the Stokes streamfunction and pressure assume the forms

$$\psi_j = \psi_j^{(0)} + \varepsilon\psi_j^{(1)}(x,\sigma,t) + \cdots, \qquad p_j = p^{(0)} + \varepsilon\, p_j^{(1)}(x,\sigma,t) + \cdots, \tag{3.2}$$

where the superscript (0) denotes the basic unidirectional flow, and the superscript (1) denotes the perturbation. The x and σ disturbance velocity components in the jth fluid derive from the Stokes streamfunction using the relations

$$w_j^{(1)} = \frac{1}{\sigma}\frac{\partial\psi_j^{(1)}}{\partial\sigma}, \qquad u_j^{(1)} = -\frac{1}{\sigma}\frac{\partial\psi_j^{(1)}}{\partial x}. \tag{3.3}$$

Substituting (3.2) into the vorticity transport equation for axisymmetric flow and linearizing, we find

$$\frac{\partial\zeta_j^{(1)}}{\partial t} + w_j^{(0)}\frac{\partial\zeta_j^{(1)}}{\partial x} = \frac{\mu_j}{\rho}\frac{1}{\sigma}\mathscr{D}^2\left(\sigma\,\zeta_j^{(1)}\right), \qquad \mathscr{D}^2\psi_j^{(1)} = -\sigma\,\zeta_j^{(1)}, \tag{3.4}$$

where $\zeta_j^{(1)}$ is the perturbation vorticity in the jth fluid, and

$$\mathscr{D}^2 \equiv \frac{\partial^2}{\partial\sigma^2} - \frac{1}{\sigma}\frac{\partial}{\partial\sigma} + \frac{\partial^2}{\partial x^2}. \tag{3.5}$$

For a normal mode perturbation with wavenumber k and complex phase velocity $c = c_R + \mathrm{i}c_I$, the perturbation assumes the usual form

$$\left(\psi_j^{(1)},\ p_j^{(1)},\ \eta\right) = (\phi_j(\sigma),\ \mu_j\, q_j(\sigma),\ A_1)\ \exp(\mathrm{i}k[x-ct]), \tag{3.6}$$

where i is the imaginary unit. The surface tension and surfactant concentration adopt the similar forms,

$$\gamma = \gamma_0 + \varepsilon\gamma_1\exp(\mathrm{i}k[x-ct]), \qquad \Gamma = \Gamma_0 + \varepsilon\Gamma_1\exp(\mathrm{i}k[x-ct]), \tag{3.7}$$

where Γ_0 and γ_0 are the uniform values corresponding to the unperturbed cylindrical interface, and Γ_1, γ_1 are complex amplitudes. Substituting (3.6) into (3.4) and combining the two equations, we derive the axisymmetric analogue of the Orr–Sommerfeld equation,

$$\frac{\mathrm{i}k\rho}{\mu_j}\left(w_j^{(0)} - c\right)(\mathscr{D}^2 - k^2)\phi_j = (\mathscr{D}^2 - k^2)^2\phi_j. \tag{3.8}$$

Linearizing the kinematic condition at the interface, $\mathrm{D}(\sigma - f)/\mathrm{D}t = 0$, where $\mathrm{D}/\mathrm{D}t$ is the material derivative, we find

$$\frac{\partial\eta}{\partial t} + u_I\frac{\partial\eta}{\partial x} - u_1^{(1)}(\sigma = a) = 0, \tag{3.9}$$

which yields the condition,

$$a(u_I - c)\,A_1 + \phi_1(a) = 0. \tag{3.10}$$

Requiring that the velocity be continuous across the interface yields the conditions

$$\phi_1 = \phi_2, \qquad \phi_1' - \phi_2' = \frac{2a^2}{(b^2 - a^2)}\, u_I\, (\lambda - 1)\, A_1, \tag{3.11}$$

where a prime indicates differentiation with respect to σ, $\lambda = \mu_2/\mu_1$ is the viscosity ratio, and all terms are evaluated at $\sigma = a$.

The linearized normal component of the interfacial stress balance (2.3) may be written in the pressure-free form,

$$\left[2\mu_j \frac{\partial^2 u_j^{(1)}}{\partial\sigma\,\partial x} - \mu_j\, \nabla^2 w_j^{(1)}\right]_2^1 = \gamma_0\left(\frac{1}{a^2}\frac{\partial\eta}{\partial x} + \frac{\partial^3\eta}{\partial x^3}\right) - \frac{1}{a}\frac{\partial\gamma}{\partial x}, \tag{3.12}$$

where all terms are evaluated at $\sigma = a$, and $[\,\cdot\,]_2^1 = [\,\cdot\,]_{j=1} - [\,\cdot\,]_{j=2}$. Note that, in the linear approximation, the effect of the Marangoni traction expressed by the last term on the right-hand side involves the stabilizing azimuthal curvature of the cylindrical configuration, but not the destabilizing perturbation curvature in an axial plane. To derive this equation, we have eliminated the pressure using the x component of the Navier–Stokes equation. Substituting the normal mode forms, we obtain

$$\begin{aligned} -2k^2\mu_1(1-\lambda)\phi_1 + \frac{1}{a}(3k^2a^2 - 1)(\mu_1\phi_1' - \mu_2\phi_2') + (\mu_1\phi_1'' - \mu_2\phi_2'') \\ -a(\mu_1\phi_1''' - \mu_2\phi_2''') = \mathrm{i}k(1 - k^2a^2)\gamma_0\, A_1 - \mathrm{i}ka\gamma_1. \end{aligned} \tag{3.13}$$

The linearized shear stress balance at the interface takes the form

$$\left[\mu_j\left(\frac{\partial w_j^{(1)}}{\partial\sigma} + \frac{\partial u_j^{(1)}}{\partial x} + \eta\frac{\mathrm{d}^2 w_j^{(0)}}{\mathrm{d}\sigma^2}\right)\right]_2^1 = \frac{\partial\gamma}{\partial x}, \tag{3.14}$$

where all terms are evaluated at $\sigma = a$. Substituting the normal mode forms we obtain

$$k^2 a\mu_1(1-\lambda)\phi_1 - (\mu_1\phi_1' - \mu_2\phi_2') + a(\mu_1\phi_1'' - \mu_2\phi_2'') = \mathrm{i}ka^2\gamma_1.$$

Finally, the linearized form of the surfactant transport equation (2.4) takes the form

$$\frac{\partial\Gamma}{\partial t} + u_I\frac{\partial\Gamma}{\partial x} + \Gamma_0\left(\frac{\partial w_1^{(1)}}{\partial x} + \frac{\partial w_1^{(0)}}{\partial\sigma}\frac{\partial\eta}{\partial x} + \frac{u_1^{(1)}}{a}\right) = D_s\,\frac{\partial^2\Gamma}{\partial x^2}, \tag{3.15}$$

where all terms are evaluated at the unperturbed position, $\sigma = a$ (e.g. Blyth & Pozrikidis 2004*a*). Substituting in this expression the normal forms (3.6) and (3.7) we find

$$\frac{\Gamma_1}{\Gamma_0} = \frac{\phi_1 - a\phi_1' - a^2 S\, A_1}{a^2(u_I - c) - \mathrm{i}ka^2 D_s}, \tag{3.16}$$

where

$$S \equiv \left(\frac{\mathrm{d}w_1^{(0)}}{\mathrm{d}\sigma}\right)_{\sigma=a} = -\frac{2\lambda a u_I}{(b^2 - a^2)}. \tag{3.17}$$

Next, we adopt the linear surface equation of state (2.2), and find $\gamma_1 = -(Ma\gamma_0/\Gamma_0)\Gamma_1$, which can be used together with (3.16) to eliminate γ_1 from the normal and tangential stress balances (3.13) and (3.15). To conclude the formulation of the linear stability problem, we require

$$\phi_1(0) = \phi_1'(0) = 0, \qquad \phi_2(b) = \phi_2'(b) = 0. \tag{3.18}$$

The first two conditions ensure that both ϕ_1/σ and ϕ_1'/σ are bounded at the origin (e.g. Drazin & Reid 1981, p. 217); the last two conditions express the no-slip and no-penetration conditions at the tube wall.

The task is to solve the axisymmetric Orr–Sommerfeld equation (3.8) subject to conditions (3.10), (3.11), (3.13), (3.15) and (3.18). Dimensional analysis reveals that the complex phase velocity, c, depends on the reduced wavenumber kb, Marangoni number Ma, core to tube radius a/b, viscosity ratio λ, Reynolds number Re, capillary number Ca, and a dimensionless property group α, defined as

$$Re = \frac{\rho u_I b}{\mu_2}, \qquad Ca = \frac{\mu_2 u_I}{\gamma_0}, \qquad \alpha = \frac{\gamma_0 b}{\mu_2 D_s}. \tag{3.19}$$

Preziosi *et al.* (1989) introduced the group

$$J \equiv \frac{Re}{Ca} = \frac{\rho\,\gamma_0\, b}{\mu_2^2}, \tag{3.20}$$

involving the physical properties of the fluids and tube radius alone. Any two of the three dimensionless numbers Re, Ca and J, can be used to characterize the stability of the core–annular flow. An appealing feature of the property group J is that it is independent of the base-flow mean shear stress represented by $\mu_2 u_I$. Thus, by fixing J and varying Ca we are able to study the effect of convective motion. Alternatively, by fixing Ca and varying Re, we are able to investigate the role of inertia mediated by the fluid density. Results will be presented for both choices of parameters.

Numerical solutions were computed using a Chebyshev tau method (e.g. Orszag 1971; Dongarra, Straughan & Walker 1996). As a preliminary, the governing equation (3.8) is multiplied by σ^4 to avoid singular coefficients at the tube axis, $\sigma = 0$, and each of the two fluid regions, $0 \leqslant \sigma \leqslant a$ and $a \leqslant \sigma \leqslant b$, is mapped onto the standard interval $-1 \leqslant \sigma_j \leqslant 1$, for $j = 1, 2$, using the linear transformations

$$\sigma_1 = 2\,\frac{\sigma}{a} - 1 \quad \text{in fluid 1}, \qquad \sigma_2 = 2\,\frac{(r-a)}{(b-a)} - 1 \quad \text{in fluid 2}. \tag{3.21}$$

The streamfunction is then expanded in a truncated series of Chebyshev polynomials, $T_k(\sigma_j)$, by setting

$$\phi_j(\sigma_j) = \sum_{k=0}^{N_j} a_{jk}\, T_k(\sigma_j), \tag{3.22}$$

for $j = 1, 2$, where a_{jk} are unknown coefficients, and N_1, N_2 are selected truncation levels. Substituting (3.22) in the axisymmetric Orr–Sommerfeld equation (3.8) for $j = 1, 2$, and projecting the result onto $T_m(\sigma_j)$ for $m = 0, \ldots, N_j - 4$ under the Chebyshev inner product,

$$\langle T_m(x),\, f(x)\rangle = \int_{-1}^{1} \frac{1}{\sqrt{1-x^2}}\, T_m(x) f(x)\, \mathrm{d}x, \tag{3.23}$$

we obtain a system of $N_1 + N_2 - 6$ linear equations for the $N_1 + N_2 + 3$ unknowns, comprised of the $N_1 + N_2 + 2$ coefficients, a_{jk}, and the interfacial amplitude A_1. All integrals involving Chebyshev polynomials and their derivatives in the projection may be computed exactly using known identities and recursive relations, as discussed in Appendix A. Substituting (3.22) into the boundary conditions (3.10), (3.11), (3.13), (3.15) and (3.18), we obtain nine more equations. This brings the total number of equations to $N_1 + N_2 + 3$, which is equal to the total number of unknowns. The

full set of equations is finally compiled in the linear system $\boldsymbol{A}\cdot\boldsymbol{w} = c\boldsymbol{B}\cdot\boldsymbol{w}$, where $\boldsymbol{w} = (a_{10}, \ldots, a_{1N_1}, a_{20}, \ldots, a_{2N_2}, A_1)^T$, and $\boldsymbol{A}$, $\boldsymbol{B}$ are square matrices of size $N_1 + N_2 + 3$. The generalized eigenvalue problem was solved using a NAG routine based on the QZ algorithm to obtain the complex phase velocities, c. To filter out spurious eigenmodes, the truncation levels N_1 and N_2 were increased until genuine modes were clearly identified. Unless otherwise stated, all results presented in the next section were computed using $N_1 = N_2 = 10$ Chebyshev modes.

A first check of the accuracy of the numerical method was performed by comparing the numerical results with those available for circular Poiseuille flow of a single fluid, and confirming excellent agreement (e.g. Davey & Drazin 1969). To gain further confidence in the spectral code, growth rates were computed for an interface that is devoid of surfactants, $Ma = 0$. Hickox (1971) showed that core–annular flow with the less viscous fluid in the core is unstable to long waves irrespective of the size of the Reynolds number. This result was extended numerically to arbitrary waves by Joseph, Renardy & Renardy (1984) in the absence of surface tension. Numerical experimentation with the present code for $\lambda > 1$ and $Ma = 0$ confirmed that the dominant mode is always unstable.

To validate the code in the presence of surfactant, the numerical results were compared with analytical expressions for Stokes flow, as discussed in Appendix B. Figure 2(a) shows a graph of the dimensionless growth rate of the dominant unstable mode $s \equiv bkc_I/u_I$, for $Ma = 1.0$, $a/b = 0.5$, $\lambda = 0.5$, $D_s = 0$, over a range of wavenumber. The solid line, corresponding to the Chebyshev tau method with Reynolds number set to zero, passes precisely through the circles representing the analytical results for Stokes flow. As a final check, the growth rates were confirmed to be identical with those computed by Kwak & Pozrikidis (2001) for a quiescent basic state, $\chi = 0$, in the presence of surfactants, under a broad range of conditions.

4. Linear stability of the core–annular flow

In the absence of surfactant, the core fluid is susceptible to the Rayleigh capillary instability when subjected to disturbances with wavenumber below a critical value. For the parameter values shown in figure 2 for Stokes flow, the surfactant raises this critical value from 2 to 2.02, and thereby extends the range of unstable wavenumber. As the capillary number increases, the effect of the surfactant becomes more pronounced. This is shown in figure 2(b), where the growth rate is plotted against wavenumber for three different values of Ca. For sufficiently large Ca, it appears that the surfactant destabilizes all wavenumbers. These predictions are in agreement with the results of Wei (2005) and Wei & Rumschitzki (2005) who studied the stability of the flow in the thin annulus limit.

In the remainder of this section, we focus our attention on the effect of inertia for moderate capillary numbers. Figure 3 illustrates the effect of the Reynolds number on the growth rate of a perturbation with wave number $kb = 1.0$, for $a/b = 0.5$, $\lambda = 0.5$ and $D_s = 0$. Results are shown both for a clean interface (dotted line), $Ma = 0$, and for a contaminated interface with $Ma = 1.0$ (solid and broken lines). At non-zero Reynolds number, an infinite number of normal modes arise. In the presence of surfactant, two most important modes can be identified. The first mode, referred to as the capillary mode, extends the corresponding dominant mode for a clean interface. The second mode, referred to as the Marangoni mode, is identified from the stability analysis for Stokes flow where precisely two normal modes arise. All three curves in figure 3 emanate from their predicted values for Stokes flow (see Appendix B).

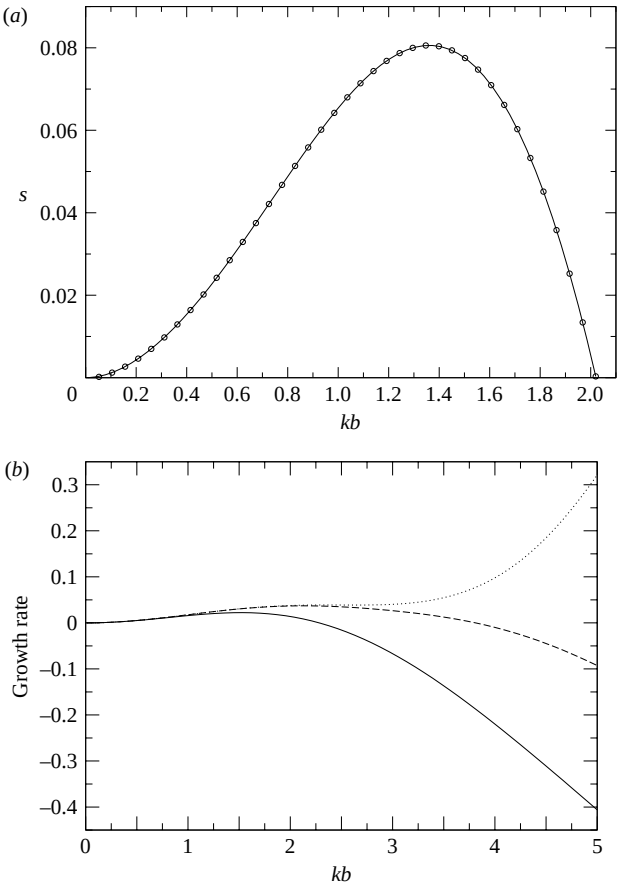

FIGURE 2. Dimensionless growth rates, $s \equiv kbc_1/u_1$, versus wave number kb for Stokes flow, $Re = 0$: (*a*) $Ca = 0.1875$, $Ma = 1.0$, $a/b = 0.5$, $\lambda = 0.5$ and $D_s = 0$. The solid line shows numerical results obtained by the tau method, and the circles represent analytical results for Stokes flow; (*b*) $Ma = 1.0$, $a/b = 0.5$, $\lambda = 0.5$, $D_s = 0$, for $Ca = 1$ (solid line showing s), $Ca = 10$ (broken line showing 10 s) and $Ca = 100$ (dotted line showing 100 s).

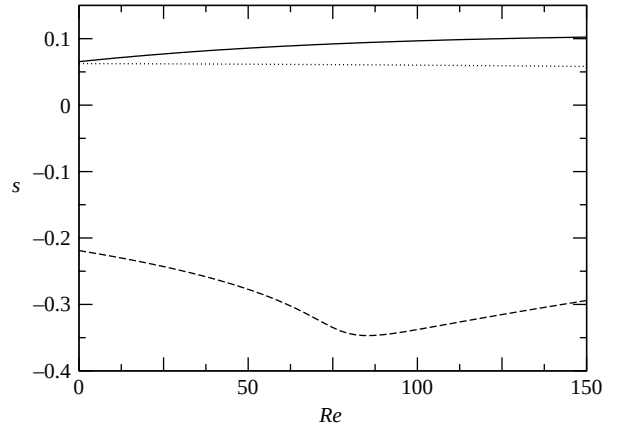

FIGURE 3. Effect of the Reynolds number on the growth rate of a wave with $kb = 1.0$, for $a/b = 0.5$, $\lambda = 0.5$, $Ca = 0.1875$, $D_s = 0$, $Ma = 0$, and $Ma = 1.0$. The dominant capillary mode in the absence of surfactants, $Ma = 0$, is shown as a dotted line, and the capillary and Marangoni for $Ma = 1.0$ are shown as solid and dashed lines, respectively.

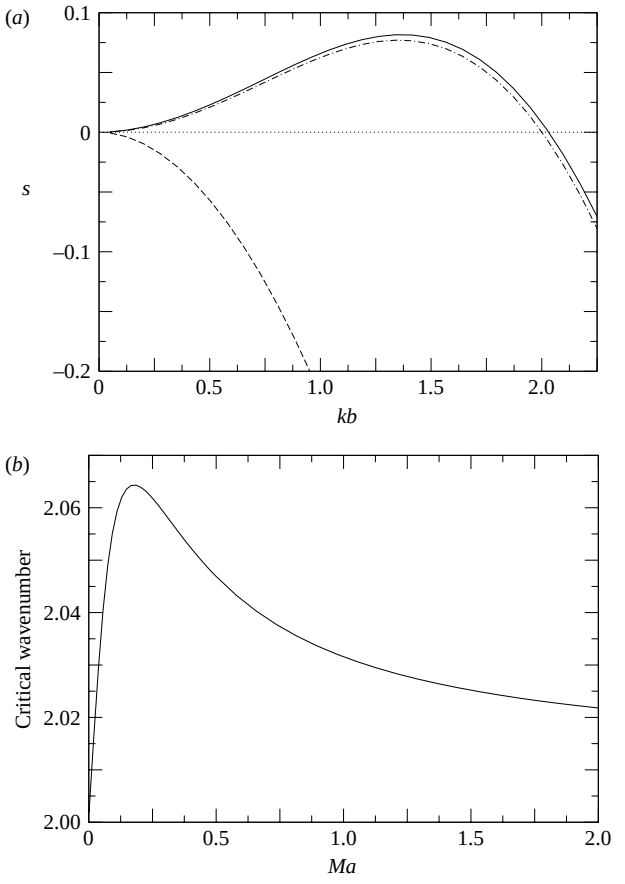

FIGURE 4. (*a*) Stability graph of a flow with $a/b = 0.5$, $\lambda = 0.5$, $D_s = 0$, $Ca = 0.1875$, $Re = 1.0$, for $Ma = 0$ and $Ma = 1.0$. The capillary and Marangoni mode for $Ma = 1.0$ are shown as solid and dashed lines, respectively, and the dominant mode for $Ma = 0$ is shown as a dot-dashed line. (*b*) Dependence of the cutoff critical wavenumber on the Marangoni number for the flow conditions considered in (*a*).

Since the reduced wave number is less than unity, $ka = 0.5$, the cylindrical interface is susceptible to the Rayleigh capillary instability. The numerical results confirm that the growth rate is positive over the range of Reynolds numbers considered. When surfactant is introduced, the dominant growth rate increases, thereby exacerbating the instability. Because the growth rate of the Marangoni growth rate is negative, the surfactant is responsible for introducing a stable normal mode.

Figure 4(*a*) shows a stability graph for $a/b = 0.5$, $\lambda = 0.5$, $D_s = 0$, and $Re = 1.0$, in the absence of surfactant, $Ma = 0$, and in the presence of surfactant, $Ma = 1.0$. The dominant growth rate for a clean interface, represented by the dot-dashed line, lies below that for a contaminated interface, represented by the solid line, over an extensive range of wavenumbers, though the differences are small. Specifically, over the range of wavenumbers shown, the maximum difference occurs at $kb = 2.25$, whereupon the growth rate in the presence of surfactant is 12.4 % larger than that for a clean interface. The growth rate of the Marangoni mode, represented by the broken line, rapidly decreases towards negative infinity as the wave number is increased. Similar

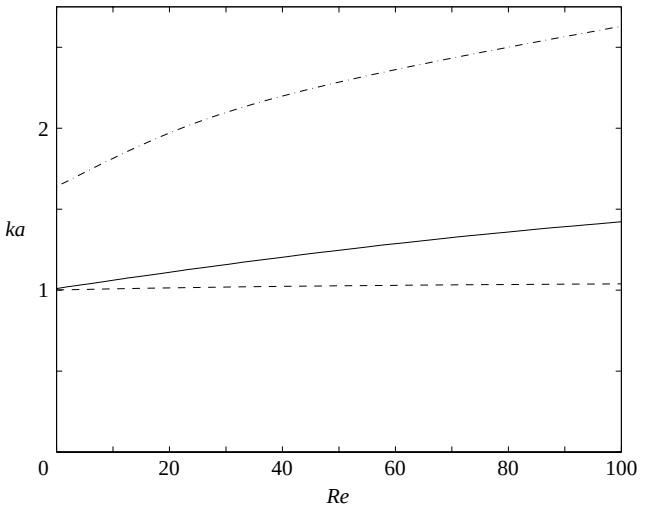

FIGURE 5. Neutral stability curves for $\lambda = 0.5$, $Ca = 0.1875$, $Ma = 1.0$, $D_s = 0$, and $a/b = 0.25$ (broken line), $a/b = 0.5$ (solid line), and $a/b = 0.75$ (dot-dashed line). Wavenumbers below each individual curve are unstable, and wavenumbers above are stable.

behaviour is observed in the case of two-layer flow in a channel confined between two parallel walls (Blyth & Pozrikidis 2004*b*).

When $a/b = 0.5$, the critical wavenumber for stability in Stokes flow in the absence of surfactant is $kb = 2.0$ for any viscosity ratio, corresponding to the Rayleigh–Tomotika threshold, $ka = 1.0$. When $Re = 1.0$ and $\lambda = 0.5$, the critical threshold is shifted slightly to $kb = 2.001$ in the absence of surfactant, and to $kb = 2.03$ in the presence of surfactant. Thus, the surfactant allows a narrow band of slightly shorter waves to grow. The effect of the Marangoni number on the critical cutoff wavenumber is demonstrated in figure 4(*b*). The maximum critical value occurs when $Ma = 0.178$, whereupon the effect of the surfactant is most significant. Figure 4 reveals that there is at most one normal mode with a positive growth rate for a given set of conditions. Extensive investigation over a wide range of parameter values failed to reveal a case where more than one growth rate is positive. This appears to be a special feature of the axisymmetric flow, and is in sharp contrast with the corresponding two-dimensional two-layer channel flow, where an exchange of stabilities may occur between the first two modes as the wave number is raised (Blyth & Pozrikidis 2004*b*).

Figure 5 shows neutral stability curves delineating the boundary between stable and unstable regimes in the Reynolds-number/wavenumber plane, for $\lambda = 0.5$, $Ma = 1.0$ and $D_s = 0$. Results are presented for three interface to tube radius ratios, $a/b = 0.25$, 0.5 and 0.75. The capillary mode is unstable for wavenumber that lie below each curve, and stable for wavenumber that lie above each curve. As $Re \to 0$, the curve corresponding to $a/b = 0.5$, shown as a solid line, approaches the value of 1.01 predicted by linear stability for Stokes flow. In all cases, inertial effects promote the range of unstable wavenumbers.

Figure 6(*a*) illustrates the effect of the viscosity ratio on the neutral curves for $Ma = 1.0$, $D_s = 0$ and $a/b = 0.5$. Results are shown for viscosity ratios $\lambda =$ 0.125, 0.25, 0.5, 1.0, 2.0 and 4.0. As in figure 5, the flow is unstable for wavenumbers that lie below each curve, and stable for wavenumber that lie above each curve. The main effect of raising the viscosity ratio is to elevate the neutral curve, and thereby

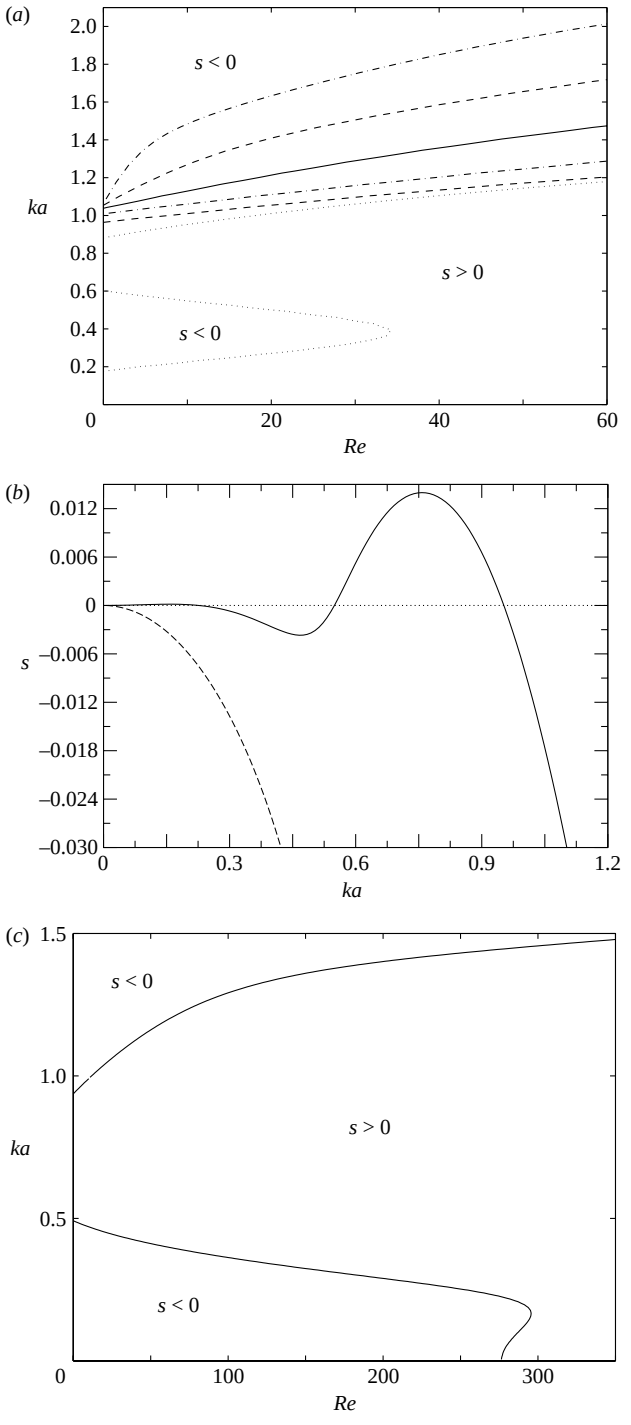

FIGURE 6. (*a*) Neutral stability curves for $Ca = 0.1875$, $Ma = 1.0$, $D_s = 0$, $a/b = 0.5$ and viscosity ratios $\lambda = 0.125$ (entire dotted line), $\lambda = 0.25$ (lower broken line), $\lambda = 0.5$ (lower dot-dashed line), $\lambda = 1.0$ (solid line), $\lambda = 2.0$ (upper broken line), $\lambda = 4.0$ (upper dot-dashed line). The annotations show regions of stability for the case $\lambda = 0.125$. (*b*) Growth rates, s, for $\lambda = 0.125$ for $Re = 10.0$. The dominant first mode appears as a solid line, and the second mode as a broken line. (*c*) Neutral stability curves for case $Ca = 0.1875$, $Ma = 1.5$, $D_s = 0$, $a/b = 0.5$ and $\lambda = 0.125$.

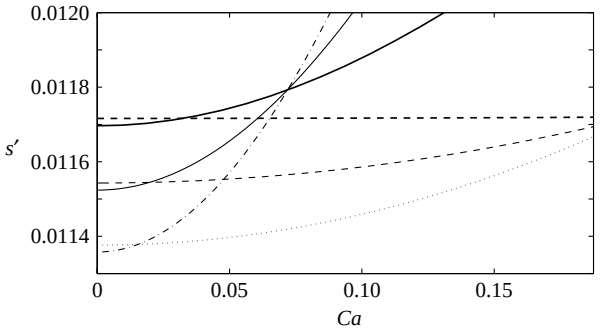

FIGURE 7. Effect of the surfactant on the dominant dimensionless growth rate, $s' \equiv Ca\, s = kbc_I\mu_2/\gamma_0$ for $a/b = 0.5$, $\lambda = 0.5$, $kb = 1$, $D_s = 0$, and $J = 1$, $Ma = 1$ (thick solid line), $J = 1$, $Ma = 0$ (thick dashed line), $J = 50$, $Ma = 1$ (solid line), $J = 50$, $Ma = 0$ (dashed line), $J = 100$, $Ma = 1$ (dash-dotted line), $J = 100$, $Ma = 0$ (dotted line).

extend the range of unstable wavenumber at a given Reynolds number. In this sense, increasing λ has a destabilizing influence independent of the surfactant.

An interesting case arises when $\lambda = 0.125$. As in the previous examples, stable and unstable modes are separated by a monotonically rising upper neutral branch, but now a hoop of stable modes is included in the space below, extending from $Re = 0.0$ to 34.4. The variation of the growth rates with wave number for the sample Reynolds number $Re = 10.0$ lying inside the range of the hoop is illustrated in figure 6(*b*). Similar isolated regions of stable modes lying beneath the upper branch of the neutral curve are also encountered in the case of a two-dimensional interface, although with a different boundary topology (Blyth & Pozrikidis 2004*b*). Increasing the Marangoni number extends the hoop to the right, as shown in figure 6(*c*) for $Ma = 1.5$, $D_s = 0$, $a/b = 0.5$ and $\lambda = 0.125$. In this example, the lower branch touches the Re axis at $Re = 276$. The critical point at the nose of the stable hoop occurs at $(kb, Re) = (0.17, 296)$. Increasing the Marangoni number shifts the critical point further to the right.

Our results have shown that the surfactant increases the growth rate of the dominant capillary mode and therefore has a destabilizing effect on the flow. In the absence of a mean flow, surfactants are known to have a stabilizing effect by decreasing the growth rate of capillary waves (Otis *et al.* 1993; Cassidy *et al.* 1999; Kwak & Pozrikidis 2001). To reconcile these predictions, we fix the property group, J, and increase the capillary number from zero so as to monitor the effect of convection on a previously quiescent configuration. Figure 7 shows a graph of the new dimensionless growth rate, $s' \equiv s\, Ca = bkc_I\mu_2/\gamma_0$, plotted against Ca, for $J = 1$, 50 and 100. In the absence of a mean flow, $Ca = 0$, the growth rate of the contaminated interface is lower than that of the clean interface for any value of J, as predicted by Kwak & Pozrikidis (2001). However, the situation is eventually reversed when the capillary number is sufficiently increased. At higher values of Ca, the growth rates for a contaminated interface are larger than those for a clean interface.

Preziosi *et al.* (1989) performed a linear stability analysis for a clean interface and presented neutral curves for fixed values of J. In figure 8, we display with the broken line the neutral curve obtained when $J = 1.0695 \times 10^5$, $\lambda = 0.1$, $a/b = 0.8696$ and $Ma = 0$, which corresponds to the conditions used to produce their figure 8. To be consistent with their dimensionless variables, we have used the alternative Reynolds number $Re_P \equiv \rho u_x(0)a/\mu_1$, which is based on the centreline velocity of the basic flow,

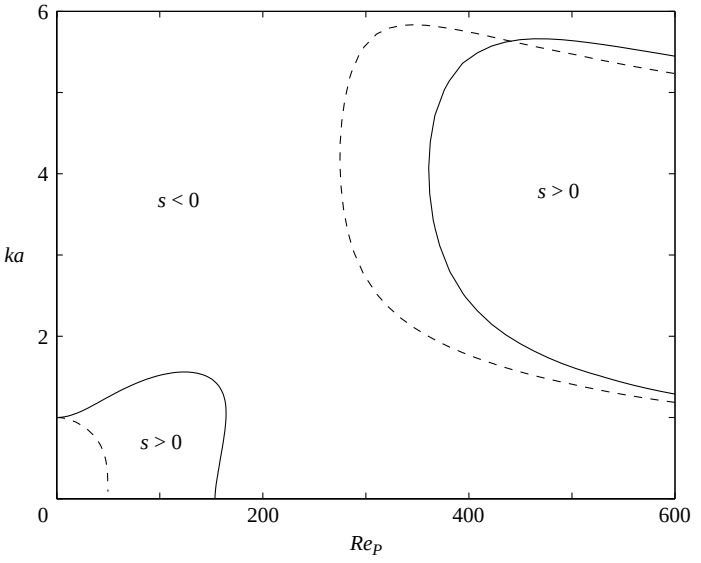

FIGURE 8. Neutral curves for $J = 1.0695 \times 10^5$, $\lambda = 0.1$, $a/b = 0.8696$, $D_s = 0$ with $Ma = 0$, shown as a broken line, and $Ma = 0.5$, shown as a solid line. The horizontal coordinate, Re_P, is defined in the text. $N_1 = N_2 = 15$ Chebyshev modes are required to resolve the upper branches accurately.

$u_x(0)$. As a result of the different choice for the velocity scale, our quoted value of J corresponds to the value of their parameter $J^* = 930$. Our figure faithfully reproduces the neutral curve presented by the previous authors in the absence of surfactant. In this case, $N_1 = N_2 = 15$ Chebyshev modes are required to resolve the upper branch accurately. Modes contained within the lower branch correspond to a long-wave instability. The lower branch joins the vertical axis at $ka = 1$, corresponding to the Rayleigh–Tomotika threshold, and crosses the horizontal axis at $Re_P = 50$. Modes to the right of the upper branch, starting at the critical value $Re_P = 275$, correspond to a shorter wave instability, and modes between the two branches are stable. Similar remarks can be made in the presence of surfactant, as illustrated by the neutral curve corresponding to $Ma = 0.5$, shown as a solid line. For this curve, the lower branch joins the horizontal axis at $Re_P = 154$, and the critical Reynolds number for the upper branch is $Re_P = 361$. Thus, the surfactant extends the range of the long-wave instability, and delays the onset of the shorter wave instability.

5. Immersed interface method

In the second part of our investigation, we consider the nonlinear evolution of axisymmetric perturbations by solving the governing equations using numerical methods. The fluid motion in an azimuthal plane is governed by the generalized Navier–Stokes equation incorporating viscosity and density differences as well as the jump in the traction across the interface owing to the surface tension,

$$\rho\left(\frac{\partial \boldsymbol{u}}{\partial t} + \boldsymbol{u}\cdot\nabla\boldsymbol{u}\right) = -\nabla p + 2\nabla\cdot(\mu\boldsymbol{E}) - \int_I \mathscr{D}_2(\boldsymbol{x}-\boldsymbol{x}')\Delta\boldsymbol{f}(\boldsymbol{x}')\,\mathrm{d}l(\boldsymbol{x}'), \qquad (5.1)$$

where $\boldsymbol{E} = (\nabla\boldsymbol{u} + \nabla\boldsymbol{u}^T)/2$ is the rate-of-deformation tensor, $\mathscr{D}_2$ is Dirac's delta function in the (x, σ)-plane with units of inverse squared length, and l is the arclength along

the trace of the interface in the (x, σ)-plane, denoted by I. The jump in the interfacial traction, $\Delta \boldsymbol{f}$, is defined in (2.3) (e.g. Pozrikidis 1997). It is reckoned that the physical properties of the fluid undergo a step discontinuity across the interface.

Using vector identities, we find that the deviatoric part of the stress tensor in three-dimensional, axisymmetric or two-dimensional flow can be expressed as

$$2\,\nabla\cdot(\mu \boldsymbol{E}) = \mu\nabla^2\boldsymbol{u} + \nabla\mu \times \boldsymbol{\omega} + 2\,\nabla\mu\cdot\nabla\boldsymbol{u}, \tag{5.2}$$

where $\boldsymbol{\omega} \equiv \nabla \times \boldsymbol{u}$ is the vorticity. The second and third terms on the right-hand side of (5.2) are non-zero only along the interface. Because $\nabla\mu$ is normal to the interface, the second term makes a contribution that is tangential to the interface and is independent of the normal component of the vorticity.

In the numerical approximation, the discontinuous density and viscosity fields are replaced by smoothed distributions defined in terms of a mollifying function $c(x, \sigma)$, which takes the value of zero in the bulk of the core fluid, the value of unity in the bulk of the annular layer, and undergoes a rapid transition across the interface. The mollified viscosity field is described as $\mu(\boldsymbol{x}) = \mu_1 + (\mu_2 - \mu_1)\, c(\boldsymbol{x})$, and the density is given by a corresponding expression. The mollifying function can be computed most efficiently on the basis of the following exact integral representation for the gradient,

$$\nabla c(\boldsymbol{x}) = -\int_I \mathscr{D}_2(\boldsymbol{x} - \boldsymbol{x}')\ \boldsymbol{n}(\boldsymbol{x}')\ \mathrm{d}l(\boldsymbol{x}'). \tag{5.3}$$

Taking the divergence of (5.3), we derive a Poisson equation for c, which is solved subject to the condition, $c = 0$ at the centreline, and $c = 1$ at the tube wall. The delta function can be further approximated with a smooth but narrowly distributed function, and the solution of the discrete problem can be found using a finite-difference method on the grid used for solving the equation of motion, as will be discussed later in this section.

In the numerical representation, one period of the interface is traced with N_I interfacial nodes, denoted as $\boldsymbol{x}_k$, $k = 1, 2, \ldots, N_I$. At each time step, the nodes are adaptively redistributed to ensure adequate spatial resolution and prevent clustering and excessive separation, as discussed by Pozrikidis (2004*b*). The shape of the interface is reconstructed from the interfacial nodes using cubic-spline interpolation with periodic boundary conditions for the first and second derivatives of the functions $x(l_p)$ and $\sigma(l_p)$. At the nodes, the interpolation variable l_p is identified with the current length of the polygonal line connecting adjacent nodes, measured from the first node. After the interpolation has been concluded, the normal and tangential vectors are computed using standard formulae of differential geometry, and the mean curvature is calculated using the formula

$$\kappa_m = -\frac{1}{2}\left(\frac{x''\sigma' - \sigma''x'}{(x'^2 + \sigma'^2)^{3/2}} + \frac{x'}{\sigma(x'^2 + \sigma'^2)^{1/2}}\right), \tag{5.4}$$

where a prime denotes a derivative with respect to the interpolation variable, l_p. The negative of the first term inside the large parentheses on the right-hand side is the curvature of the interface in the (x, σ)-plane, and the negative of the second term is the conjugate curvature.

In the immersed-interface method (IIM) inspired by Peskin's immersed-boundary method (IBM) (Peskin 2002) and coined 'front tracking' by some subsequent authors (e.g. Tryggvason *et al.* 2001), the line integral on the right-hand side of (5.1) is

approximated using the trapezoidal rule, yielding

$$\int_I \mathscr{D}_2(\boldsymbol{x}-\boldsymbol{x}')\Delta\boldsymbol{f}(\boldsymbol{x}')\,\mathrm{d}l(\boldsymbol{x}') \simeq \sum_{k=1}^{N_I} \mathscr{D}_2(\boldsymbol{x}-\boldsymbol{x}_k)\Delta\boldsymbol{f}_k \frac{l_{k+1}-l_{k-1}}{2}. \tag{5.5}$$

In computing $\Delta\boldsymbol{f}_k$, the Marangoni traction expressed by the second term on the right-hand side of (2.3) is evaluated using cubic-spline interpolation with respect to the polygonal arclength, l_p, as $\partial\gamma/\partial l = (\partial\gamma/\partial l_p)(\partial l_p/\partial l)$. Moreover, the delta function associated with each node is replaced by a smooth function supported by a rectangular region centred at the node. For the kth node, we introduce the approximation

$$\mathscr{D}_2(\boldsymbol{x}-\boldsymbol{x}_k) \simeq \mathscr{H}(\boldsymbol{x}-\boldsymbol{x}_k) \equiv \frac{1}{16\,\delta_1\delta_2}(1+\cos\hat{x})(1+\cos\hat{\sigma}), \tag{5.6}$$

for $|x-x_k| < 2\delta_1$ and $|\sigma-\sigma_k| < 2\delta_2$, where $\delta_1 \equiv (\Delta x)^q$, $\delta_2 \equiv (\Delta\sigma)^q$, Δx and $\Delta\sigma$ are spatial discretization intervals in the streamwise and radial direction associated with the finite-difference method, $0 < q \leqslant 1$ is a parameter that determines the spreading length, and

$$\hat{x} \equiv \frac{\pi(x-x_k)}{2\,\delta_1}, \qquad \hat{\sigma} \equiv \frac{\pi(\sigma-\sigma_k)}{2\,\delta_2}. \tag{5.7}$$

In particular, the approximate delta function (5.6) spreads over a rectangular area whose size is equal to $4\,\delta_1$ in the x-direction and $4\,\delta_2$ in the σ-direction. When $q=1$, $\delta_1 = \Delta x$ and $\delta_2 = \Delta\sigma$. As the grid is refined, δ_1 and δ_2 decrease in proportion with Δx and $\Delta\sigma$, and the approximate delta function becomes more narrowly distributed. However, when $q < 1$, δ_1 and δ_2 decrease slower than Δx and $\Delta\sigma$. Consequently, the approximate delta function occupies a higher number of grid intervals as the grid is refined. To ensure a smooth velocity field, the delta function must be better resolved as the grid becomes finer. Numerical experimentation showed that $0.6 \leqslant q \leqslant 0.8$ is appropriate for the simulations discussed in the next section.

To compute the evolution of the flow subject to an initial condition, we use a variation of Chorin's projection method. The algorithm involves a number of elementary sub-steps based on the constituent evolution equations

$$\rho\frac{\partial\boldsymbol{u}}{\partial t} = -\chi\,\boldsymbol{e}_x + \nabla\mu\times\boldsymbol{\omega} + \mathscr{B}(\boldsymbol{x}), \tag{5.8a}$$

$$\rho\left(\frac{\partial\boldsymbol{u}}{\partial t} + \boldsymbol{v}\cdot\nabla\boldsymbol{u}\right) = \mu\nabla^2\boldsymbol{u}, \qquad \rho\,\frac{\partial\boldsymbol{u}}{\partial t} = -\nabla\phi, \tag{5.8b,c}$$

where

$$\mathscr{B}(\boldsymbol{x}) \equiv -\int_I \mathscr{H}(\boldsymbol{x}-\boldsymbol{x}')\Delta\boldsymbol{f}(\boldsymbol{x}')\,\mathrm{d}l(\boldsymbol{x}'), \tag{5.9}$$

$\boldsymbol{v} \equiv \boldsymbol{u} - (2/\rho)\,\nabla\mu$, χ is a specified pressure drop across each period of length L, $\boldsymbol{e}_x$ is the unit vector along the x-axis, and ϕ is a projection function regarded as an approximation of the non-periodic part of the pressure (e.g. Pozrikidis 1997, 2003). To expedite the simulations, the second step is further decomposed into two one-dimensional convection–diffusion steps,

$$\rho\left(\frac{\partial\boldsymbol{u}}{\partial t} + v_x\frac{\partial\boldsymbol{u}}{\partial x}\right) = \mu\frac{\partial^2\boldsymbol{u}}{\partial x^2}, \qquad \rho\left(\frac{\partial\boldsymbol{u}}{\partial t} + v_\sigma\frac{\partial\boldsymbol{u}}{\partial\sigma}\right) = \mu\begin{pmatrix} \dfrac{1}{\sigma}\dfrac{\partial}{\partial\sigma}\left(\sigma\dfrac{\partial u_x}{\partial\sigma}\right) \\ \dfrac{\partial}{\partial\sigma}\left[\dfrac{1}{\sigma}\dfrac{\partial(\sigma u_\sigma)}{\partial\sigma}\right] \end{pmatrix}. \tag{5.10}$$

The first sub-step is subject to the streamwise periodicity condition, whereas the second sub-step is subject to carefully designed conditions at the tube wall and centreline, as will be discussed later in this section. The governing equations were integrated in time using a finite-difference method on a uniform grid. Specifically, (5.8*a*) was integrated using the explicit Euler method, while equations (5.10) were integrated using the implicit Crank–Nicolson method. The latter requires the solving of tridiagonal or nearly tridiagonal systems of linear equations using the standard and a modified version of the Thomas algorithm (e.g. Pozrikidis 1998).

In the computations discussed in this article, the densities of the core and annular fluids are identical. Treating the density as a constant, and demanding that (5.8*c*) delivers a solenoidal velocity field at the end of a complete time step, we derive a Poisson equation for the projection function, $\nabla^2\phi = (\rho/\Delta t)\,\nabla\cdot\boldsymbol{u}^*$, where $\boldsymbol{u}^*$ is the intermediate velocity at the end of the convection–diffusion step. The solution was found using standard Gauss–Seidel iterations, subject to the streamwise periodic condition and the homogeneous Neumann boundary condition at the channel walls.

The no-penetration boundary condition at the tube wall and symmetry condition at the centreline, $u_\sigma = 0$, are imposed in solving (5.10). To ensure the exact satisfaction of the no-slip boundary condition at the wall at the end of the projection step, advancement over each time step is carried out in an iterative fashion, wherein a slip boundary condition at the wall for the intermediate velocity at the σ convection–diffusion step is gradually modified in anticipation of the $O(\Delta t)$ slip velocity introduced in the projection step. Similarly, a non-zero slope condition for $\partial u_x/\partial\sigma$ is imposed at the centreline, and is then modified during each iteration so that the intermediate velocity field cancels the error introduced in the projection step. In practice, because both slip velocities are transferred from the previous step, only one or two iterations are necessary to reduce u_x at the wall and $\partial u_x/\partial\sigma$ at the centreline down to the level of the round-off error.

Once the velocity field has been updated over a time step, the interfacial marker points are advanced with the interpolated velocity field using Euler's explicit method. In the present numerical simulations, the interfacial nodes are chosen to be Lagrangian point particles convected with the fluid velocity. The interpolation of the nodal velocity is carried out using the bicubic B-spline approximation in the (x, σ)-plane (e.g. Pozrikidis 2004*b*). The convection–diffusion equation (2.4) is simultaneously integrated by a finite-volume method (Pozrikidis 2004*b*). In particular, following or preceding the advancement of the interfacial nodes, the concentration field is advanced in time using a semi-implicit method, where the geometrical properties of the interface are evaluated at the beginning of each time step.

The performance of the numerical method was assessed by comparing the results of numerical simulations with the predictions of linear stability theory. As a first test, we consider the stationary core–annular arrangement in the absence of surfactants, $\beta = 0$. A perturbation is introduced by displacing the interface to a position described by

$$\sigma(x, t = 0) = a + \epsilon\, b\, \cos(kx), \tag{5.11}$$

where $k = 2\pi/L$ is the wavenumber, and ϵ is the dimensionless amplitude of the disturbance.

Figure 9 shows the evolution of the interface amplitude, a_1, normalized by the initial amplitude, $a_0 \equiv \epsilon b$, plotted against the dimensionless time $\tau \equiv t\gamma_0/(\mu_2 b)$ on a log–linear scale, for $\lambda = \mu_2/\mu_1 = 0.5$ and $J = 1$, in the absence of a mean flow, $Ca = 0$. The unperturbed interface is located at $a = 0.5b$, the wavelength of the interfacial

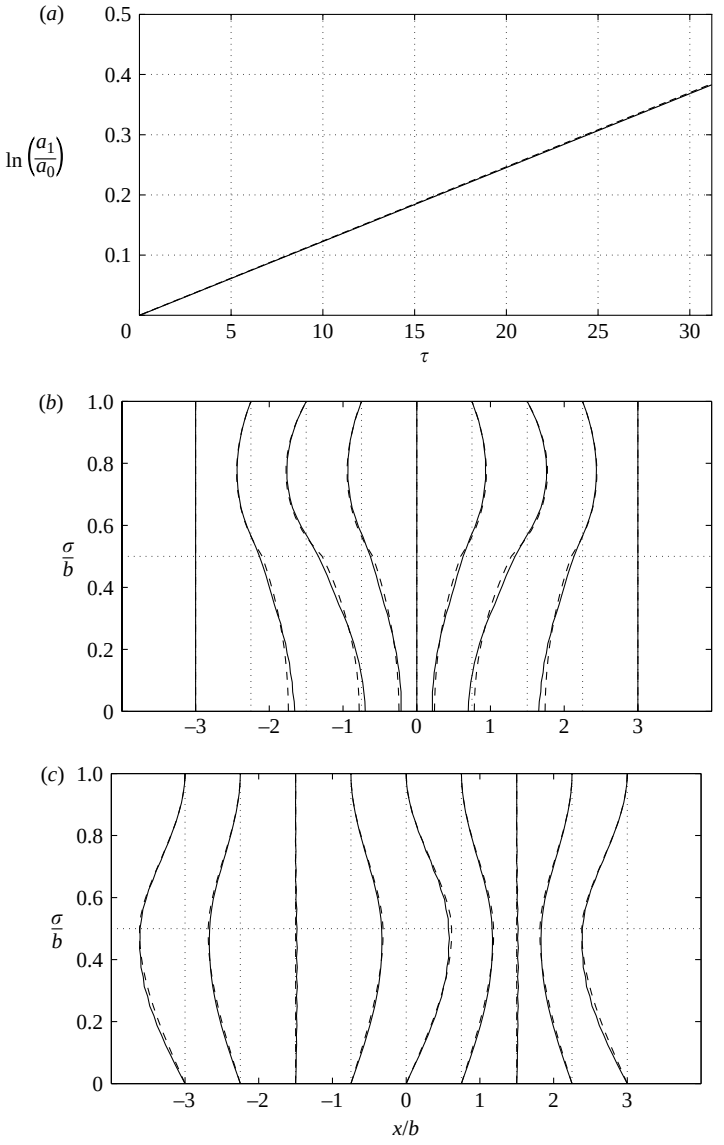

FIGURE 9. (*a*) Capillary instability of a stationary arrangement in the absence of surfactants, for $a/b = 0.5$, $L/b = 6$ and $\mu_2/\mu_1 = 0.5$. The dashed line represents the predictions of linear stability theory. (*b*, *c*) Velocity profiles at time $\tau = 0.1$ at locations $kx = -2\pi$, $-3\pi/2$, $-\pi$, $-\pi/2$, 0, $\pi/2$, π, $3\pi/2$. (*b*) u_x reduced by $10^{-3}\gamma_0/\mu_2$, and (*c*) u_σ reduced by $2 \times 10^{-4}\gamma_0/\mu_2$. The dashed lines represent the prediction of linear stability theory calculated from the velocity eigenfunctions.

wave is $L/b = 6$, the initial amplitude of the interface is $\epsilon = 0.01$, and the initial velocity is set to zero at all grid points. The simulation was conducted on a 48×24 grid in the (x, σ)-plane, with dimensionless time step $\Delta\tau = 0.005$. The dashed line with slope $s' = kbc_1\mu_2/\gamma_0 = 0.012329$ in figure 9(*a*) represents the prediction of the linear stability analysis of Kwak & Pozrikidis (2001), which describes the exponential growth of a normal mode. The numerical results are in excellent agreement with this theoretical estimate. Figure 9(*b*, *c*) shows velocity profiles calculated on a 48×32

grid at time $\tau = 0.1$, at several streamwise locations. The solid lines represent the numerical results, and the dashed lines represent the velocity profiles constructed from the eigenfunctions of the linear stability problem given by Kwak & Pozrikidis (2001). The graphs reveal that the radial velocity component, u_σ, is in phase with the interfacial wave, whereas the streamwise component, u_x, is shifted by 90°. Overall, the numerical results faithfully reproduce the eigenfunctions even though the initial condition does not precisely correspond to an eigenmode.

Next, we consider core–annular flow and compare the numerical results with the predictions of linear stability analysis discussed in § 4, in the absence of surfactants. The numerical simulations were conducted on a 96×24 grid, using the unperturbed unidirectional velocity field as an initial condition. Figure 10(a) shows the growth of the interfacial amplitude for $a/b = 0.5$, $kb = 0.5$, $Re = 0.1875$, $\lambda = 0.5$, $Ca = 0.1875$ and $\epsilon = 0.01$. The solid line representing the simulations is in excellent agreement with the dashed line with slope $s' = 0.003915$, representing the prediction of linear analysis. Because of the mean flow, the interfacial wave is convected with phase velocity $c_R \simeq 0.16\gamma_0/\mu_2$, which is in good agreement with that predicted by linear theory, $c_R = 0.169874\gamma_0/\mu_2$, and is somewhat lower than the unperturbed interfacial velocity, $u_I = 0.1875\gamma_0/\mu_2$. Figure 10($b$, c) shows the profiles of the perturbation velocity calculated on a 96×32 grid at time $\tau = 0.2$, at several streamwise locations. Note that the artificial interfacial jump in the velocity eigenfunctions is smoothed out in the simulation.

As a last case study, we consider flow in the presence of surfactants. The flow parameters are the same as those in figure 10, except that $\beta = 0.5$ and $D_s = 0$. The initial surfactant concentration is described by

$$\Gamma(x, t = 0) = \Gamma_0[1 + \epsilon_\Gamma \cos(kx - \phi_\Gamma)], \tag{5.12}$$

where Γ_0 is unperturbed surfactant concentration, ϵ_Γ is the dimensionless amplitude of the perturbation, and ϕ_Γ is the phase-shift of the surfactant concentration wave with respect to the initial interfacial displacement described by (5.11). The normal mode analysis reveals an unstable eigenmode with $\epsilon_\Gamma/\epsilon = 4.7780$ and $\phi_\Gamma = -0.3199$. A simulation with $\Gamma_0 = 1$ and $\epsilon_\Gamma = 0.01$ shows that the interfacial wave grows with growth rate $s' \simeq 0.0053$, which is close to that estimated by the linear stability analysis, $s' = 0.004268$. The numerical phase velocity, $c_R \simeq 0.16\gamma_0/\mu_2$, is in better agreement with the prediction of linear analysis, $c_R = 0.168780\gamma_0/\mu_2$.

In summary, the numerical method was confirmed to reproduce faithfully the behaviour predicted by linear stability theory for small perturbations, and may therefore be used with confidence to study the evolution of nonlinear waves.

6. Simulation of the nonlinear motion

The numerical method discussed in § 5 was applied to study the nonlinear stages of the instability of the core–annular flow beyond the confines of linear theory. In all simulations presented in this section, the undisturbed unidirectional flow was chosen as the initial condition, and the initial amplitudes of the interface and surfactant concentration waves were set to $\epsilon = 0.01$ and $\epsilon_\Gamma = 0$. Numerical experimentation revealed that the initial amplitude of the surfactant concentration does not have a profound influence on the evolution and only mildly affects the transient interfacial profiles. Both the total amount of surfactant and the individual fluid volumes are well preserved, with relative errors of less than 1% incurred throughout the simulations.

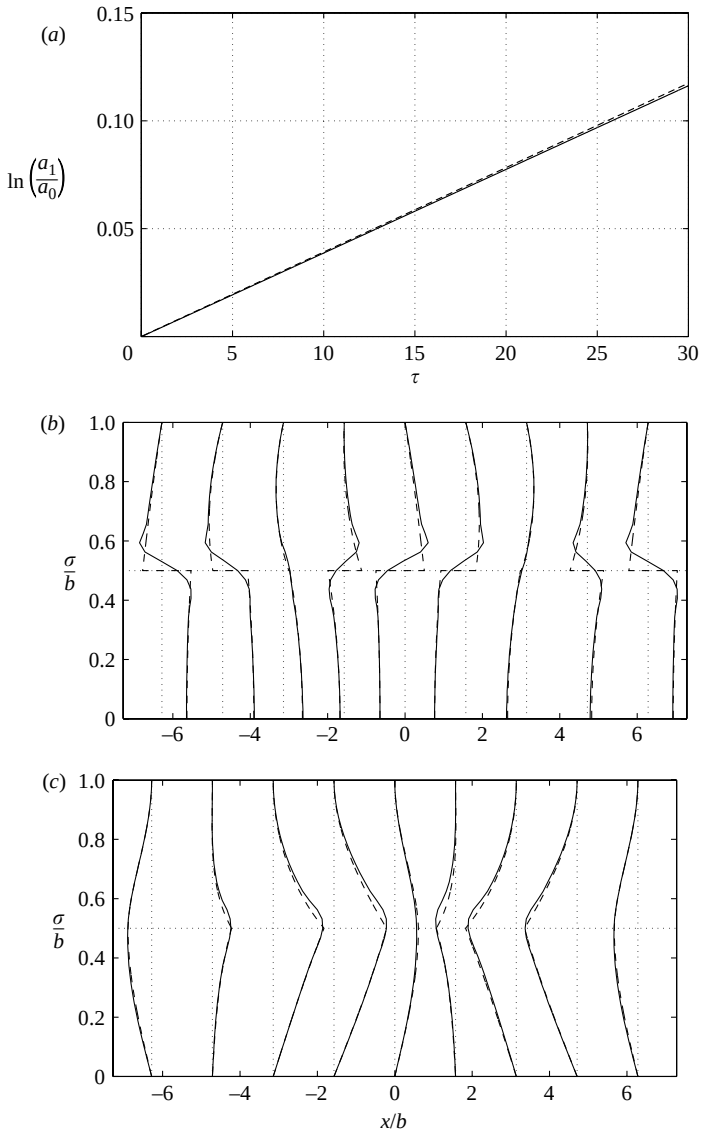

FIGURE 10. (*a*) Growth of the interfacial wave in core–annular flow in the absence of surfactants, for $a/b = 0.5$, $L/b = 6$, $\mu_2/\mu_1 = 0.5$, $Re = 0.1875$ and $Ca = 0.1875$. The dashed line represents the prediction of linear stability theory. (*b*, *c*) Profiles of velocity perturbation at time $\tau = 0.2$ at $kx = -2\pi$, $-3\pi/2$, $-\pi$, $-\pi/2$, 0, $\pi/2$, π, $3\pi/2$, and 2π. (*b*) Streamwise component reduced by $10^{-3}\gamma_0/\mu_2$; (*c*) radial component reduced by $6.6667 \times 10^{-5}\gamma_0/\mu_2$. The dashed lines represent the predictions of linear stability theory, calculated from the velocity eigenfunctions.

The growth of the interfacial amplitude is shown in figure 11 for an assortment of flow conditions, in the presence and absence of the surfactant. In all cases, the initial growth rate of the contaminated interface is close to that of the corresponding clean interface, as predicted by linear stability analysis. The effect of the surfactant becomes important at longer times. It is interesting that the clean interface sustains the linear growth rate for a long period of time, whereas the contaminated interface exhibits a nonlinear growth at an early stage of the motion. In most cases, the disturbance is

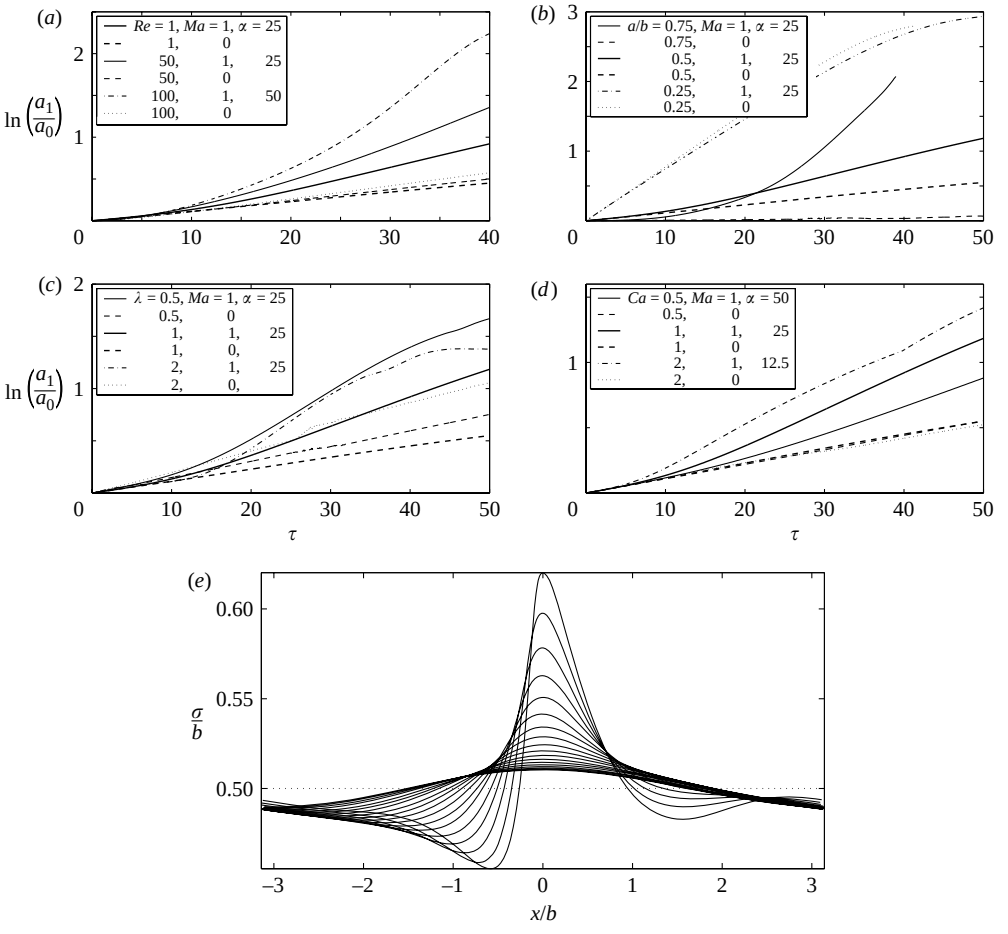

FIGURE 11. Nonlinear growth of interfacial waves with $L/b = 2\pi$ and (*a*) various Reynolds numbers for $a/b = 0.5$, $\lambda = 0.5$, $Ca = 1.0$, (*b*) various mean interface positions, a/b, for $Re = 1.0$, $\lambda = 0.5$, $Ca = 1.0$, (*c*) various viscosity ratios, λ, for $a/b = 0.5$, $Re = 1.0$, $Ca = 1.0$, and (*d*) various capillary numbers, Ca, for $Re = 1.0$, $a/b = 0.5$, $\lambda = 0.5$. Note that the two dashed lines in (*d*) are nearly indistinguishable. (*e*) Interfacial profiles for $Re = 100$, $a/b = 0.5$, $\lambda = 0.5$, $Ca = 1.0$, $L/b = 2\pi$, $\alpha = 50$ and $Ma = 1$ at times $\tau = 4, 6, 8, \ldots, 38$; the interface has been shifted so that the maximum point is located at the origin of the x-axis. The undisturbed interface is shown as a dotted line.

amplified faster in the presence of the surfactant, and this corroborates the notion that the surfactant has a destabilizing effect in the presence of a mean flow.

Figure 11(*e*) shows evolving interfacial profiles for $Re = 100$, $a/b = 0.5$, $\lambda = 0.5$, $Ca = 1.0$, $L/b = 2\pi$, $\alpha = 50$ and $Ma = 1$, over a period of time from $\tau = 4$ to 38. To illustrate clearly the evolution of the profiles, the origin of the x-axis has been shifted to the point of maximum radial deflection. During the early stage of the motion, the interface retains a regular sinusoidal profile. As the amplitude of the wave grows and nonlinearity comes into play, the crests of the developing wave tend to steepen and eventually overturn.

Figure 12 shows evolving interfacial profiles in a stationary frame of reference for a relatively thin annulus, $a/b = 0.75$, $Re = 0.5833$, $\lambda = 0.5$, $Ca = 0.5833$, $L/b = \pi$, $\alpha = 20$ and $Ma = 1$. In these illustrations, the mean flow has been filtered out to

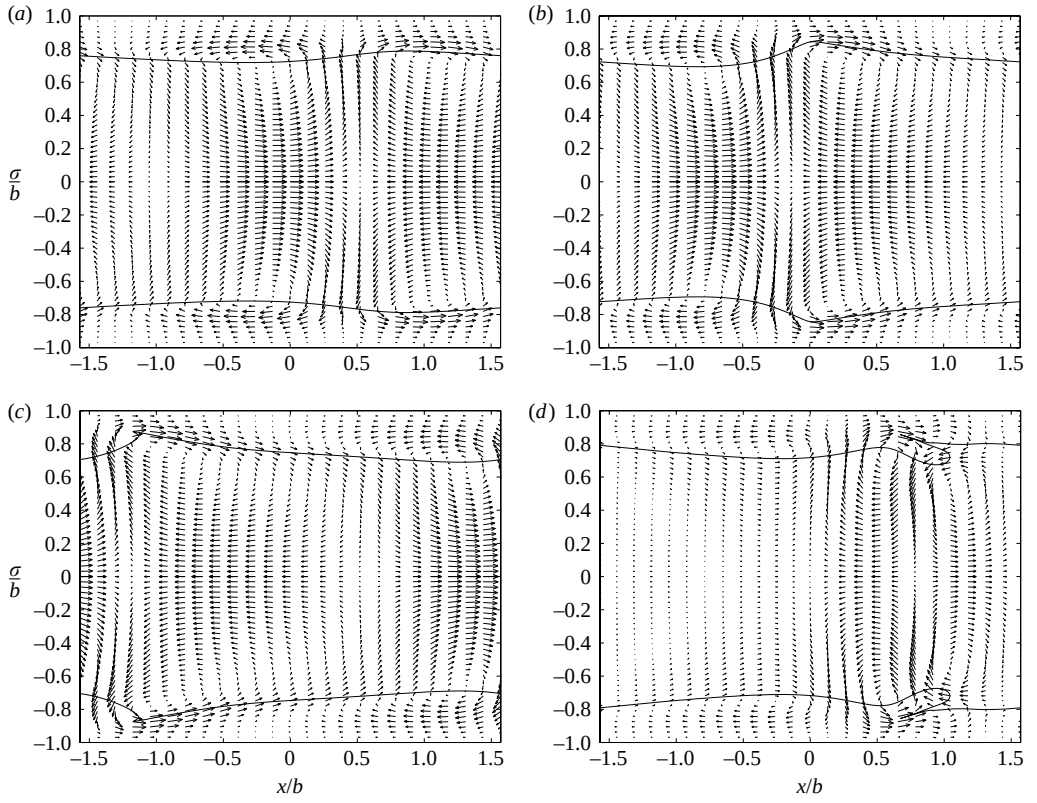

FIGURE 12. Illustration of the disturbance velocity field for $Re = 0.5833$, $a/b = 0.75$, $\lambda = 0.5$, $Ca = 0.5833$, $L/b = \pi$, $\alpha = 20$ and $Ma = 1$ at time (*a*) $\tau = 30$, (*b*) $\tau = 50$ (*c*) $\tau = 55$ and (*d*) $\tau = 60$. The interface is shown as a solid line.

reveal the disturbance velocity. Linear theory in the absence of surfactant predicts a negative dimensionless growth rate, $s' = -0.01275$, corresponding to a stable flow. Adding surfactant destabilizes the flow by raising the growth rate to the positive value $s' = 0.03653$. The nonlinear evolution leads to the development of a pointed wave. The wave does not reach a steady state, and the simulation terminates when thin wisps of the more viscous core fluid penetrate the less viscous annular fluid, whereupon the numerical method fails owing to the high curvature at the apex. In all parts of figure 12, a pair of counter-rotating vortices is evident within each wave. The velocity vectors indicate that the upstream side of the crest is moving away from the centreline, whereas the downstream side is moving toward the centreline. Thus, the interfacial wave is convected with a velocity that is lower than the unperturbed interfacial velocity, which is consistent with the predictions of the linear theory, $c_R = 0.802\, u_I$.

Figure 13 shows several stages in the evolution of a wave for flow parameters identical to those corresponding to figure 11(*b*), taking $a/b = 0.25$, $Ma = 1$ and $D_s = 0$. The profiles in figures 13(*a*) and 13(*b*) suggest that the growing wave is accompanied by a pair of counter-rotating vortices, and the interfacial wave propagates faster than the mean flow. This behaviour is consistent with the estimate of linear theory for the phase velocity, $c_R = 1.0065\, u_I$. The profiles in figures 13(*b*) and 13(*c*) indicate that the core cross-section at point B, located on the upstream side of the crest, thins as fast as the cross-section at point A, located at the trough of the wavy core flow. Figure 13(*d*)

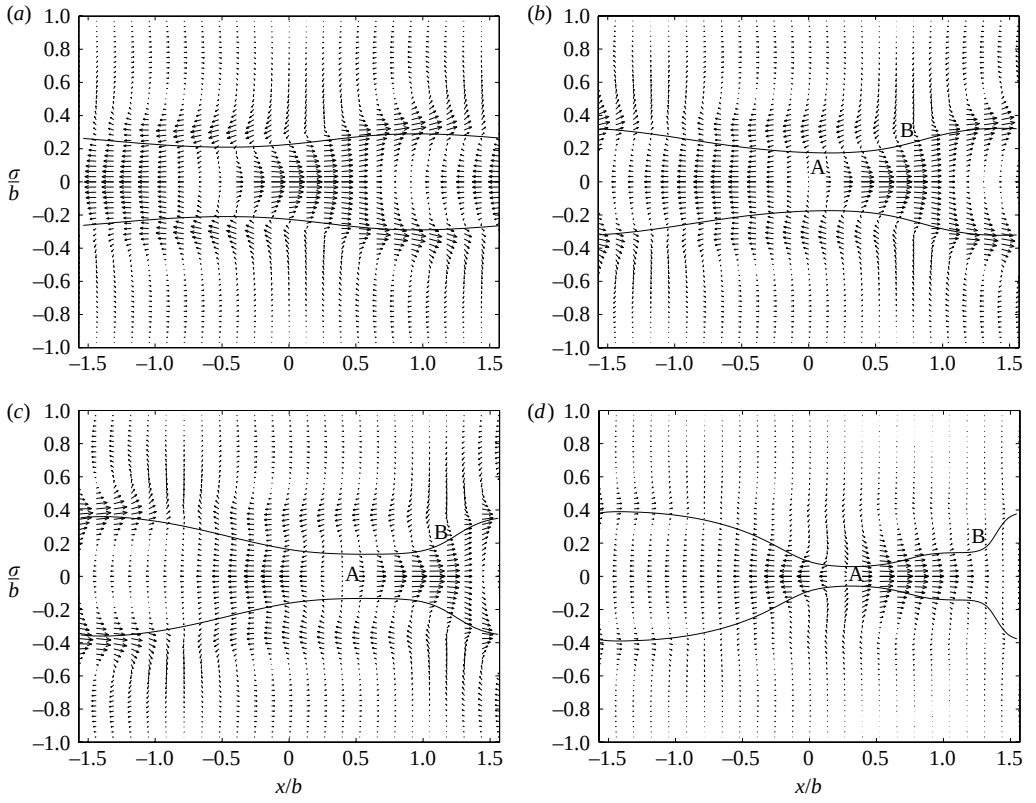

FIGURE 13. The disturbance velocity field with $Re = 1.0$, $a/b = 0.25$, $\lambda = 0.5$, $Ca = 1.0$, $L/b = \pi$, $D_s = 0$ and $Ma = 1$ at time (*a*) $\tau = 20$, (*b*) 30, (*c*) 40 and (*d*) 50. The interface is shown as a solid line.

shows that point A finally outruns point B and suggests that the core will eventually break up at point A to form an array of slugs. This example illustrates the potentially complicated dynamics of the core–annular flow in the presence of a surfactant during the nonlinear stages of the motion.

Figure 14 shows a different type of core breakup occurring at $Re = 10$, $a/b = 0.25$, $\lambda = 2$, $Ca = 0.25$, $L/b = 2\pi$, $\alpha = 50$ and $Ma = 1$. Note that, in this case, the core fluid is less viscous than the annular fluid. Linear stability analysis predicts that the core–annular flow in the absence of a surfactant is unstable to long-waves when $\lambda > 1$, regardless of the Reynolds number (Hickox 1971). The present simulation reveals that the interface evolves under action of the Marangoni traction, and the results suggest that the wave will pinch off at several locations into a series of drops suspended in the annular fluid. The size of the drops and precise protocol of core breakup cannot be determined from linear stability theory.

7. Summary

We have examined the linear and nonlinear instability of the surfactant-laden core–annular flow, subject to axisymmetric disturbances. The stability of the clean core–annular flow has received a great deal of attention in the literature. The primary

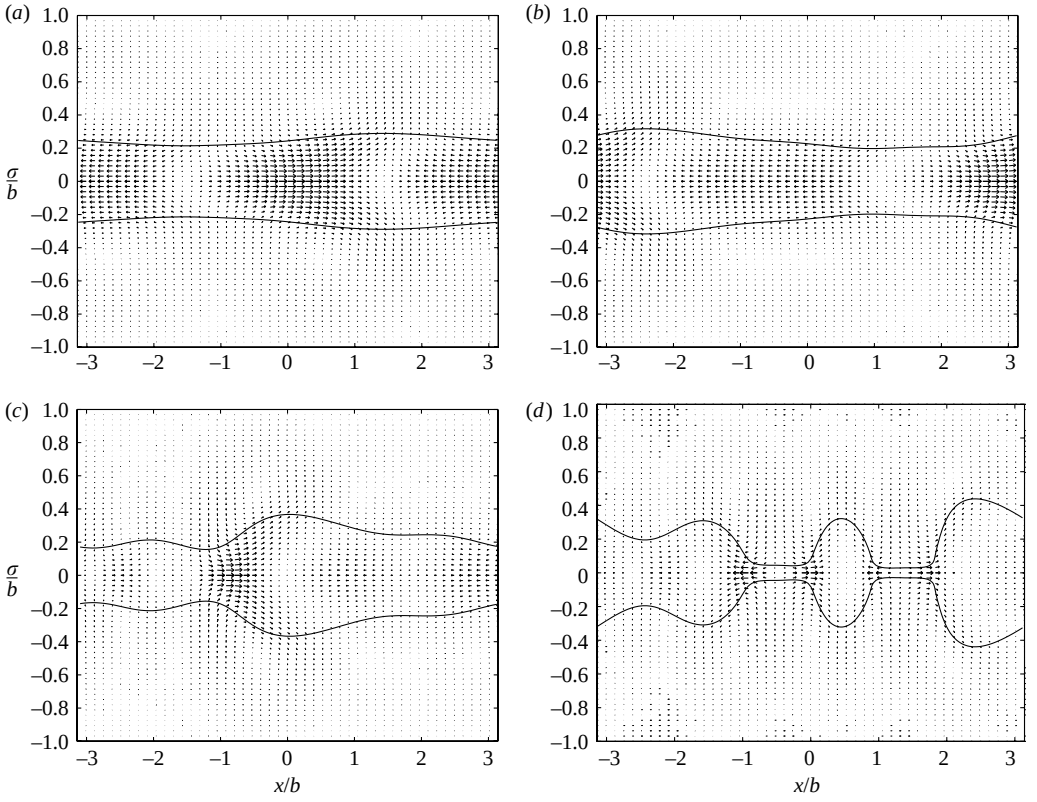

FIGURE 14. The disturbance velocity field for $Re = 10$, $a/b = 0.25$, $\lambda = 2$, $Ca = 0.25$, $L/b = 2\pi$, $\alpha = 50$ and $Ma = 1$ at time (*a*) $\tau = 30$, (*b*) 40, (*c*) 50 and (*d*) 60. The interface is shown as a solid line.

contribution of the present work is a quantified assessment of the effect of the surfactant and a description of the nonlinear dynamics by direct numerical simulation.

In the first part of the investigation, a normal-mode linear stability analysis was conducted to examine the behaviour of small-amplitude perturbations. Numerical solutions of the Orr–Sommerfeld equation were computed at arbitrary Reynolds numbers using a Chebyshev tau method. Trial calculations showed that few Chebyshev modes are required to resolve the growth rates accurately. The code was validated by successful comparison with results for Stokes flow, as well as with previous work for stationary fluids (Kwak & Pozrikidis 2001). Analytical results for Stokes flow revealed the existence of two normal modes, including the capillary mode of the cylindrical interface, and a Marangoni mode associated with the surfactant. Although an infinite number of normal modes arise at non-zero Reynolds numbers, the dominant capillary and Marangoni modes can be identified by parameter continuation with respect to the Reynolds number. We have found that only one normal mode is unstable for all conditions considered, and the capillary mode dominates and is responsible for the overall instability of the core–annular flow. This finding contrasts with results for a two-dimensional interface in two-layer channel flow, where two modes can have positive growth rates, and either may determine the instability of the flow depending on the flow parameters.

In the case of core–annular flow, the chief effect of the surfactant is to elevate the growth rate of the dominant capillary mode, and to extend the range of unstable wavenumbers. This coincides with the findings of Wei (2005) and Wei & Rumschitzki (2005), who made the same observation when the annular layer is thin. The surfactant has a most significant influence at moderate Marangoni numbers, since the cutoff wavenumber for instability quickly reaches a maximum as the Marangoni number rises. Neutral curves presented for a variety of parameter values have revealed that the range of unstable wavenumbers grows with Reynolds number when the capillary number is fixed, and this highlights the destabilizing role of inertia. The unstable range also widens by decreasing the thickness of the annular layer or by raising the viscosity ratio. Increasing the viscosity ratio above a critical level alters the topology of the neutral stability contour, with a hoop of stable modes appearing below the main neutral branch enclosing stable modes in a certain band of wavenumbers.

The effect of convection was also considered. We have noted an apparent inconsistency between the present observations in the presence of a mean flow where surfactant has a destabilizing influence, and those observed for stationary fluids where the surfactant tends to calm interfacial disturbances. The discrepancy was resolved by noting a crossover in the growth rates when the capillary number is increased from zero. Neutral curves for a fixed suitably defined surface tension parameter and varying Reynolds or capillary number reproduced previous results of Preziosi *et al.* (1989) for a clean interface, and extended them to non-zero Marangoni numbers. In the presence of a mean flow, a long-wave instability occurs at small Reynolds numbers. After a gap, this is followed by a shorter-wave instability at higher Reynolds numbers.

In the second part of the investigation, we conducted a numerical study of the nonlinear motion using a combined immersed interface method and finite-difference discretization. The code was validated by successful comparison with the present linear stability results, as well as with the results of Kwak & Pozrikidis (2001) for quiescent fluids. The numerical simulations are in excellent agreement with the normal-mode predictions in the early stages of the motion. When surfactant is present, the nonlinear dynamics exhibits a more pronounced departure from the forecasts of linear theory, as nonlinear effects quickly take hold. As the nonlinearities develop, the waves grow and may eventually steepen and overturn. Different types of evolution are observed under different flow conditions, including the development of pointed waves and arrangements suggestive of the formation of slugs and drops.

In conclusion, the surfactant has a generally destabilizing effect on the core–annular flow, and the Marangoni traction resulting from non-uniform distribution of the surfactant is responsible for a dynamics that is far more complex than that for a clean flow.

This research was supported by a grant provided by the National Science Foundation. M. G. B. was supported by the Nuffield Foundation under grant NUF-NAL-O4.

Appendix A. Calculation of the Chebyshev integrals

To compute the normal modes, the axisymmetric analogue of the Orr–Sommerfeld equation is multiplied through by σ^4 and projected onto $T_m(\sigma_j)$ for $m = 0, \ldots, N_j - 4$ in each fluid, $j = 1, 2$, in preparation for the Chebyshev tau method. The resulting equations involve integrals of the type

$$I = \int_{-1}^{1} w(x)\, T_n\, \frac{\mathrm{d}^q T_m}{\mathrm{d}x^q}\, x^p\, \mathrm{d}x \tag{A 1}$$

for integers $p \leqslant 5$, $q \leqslant 4$, and for general integers n, m, where $T_n(x)$ is a Chebyshev polynomial, and $w(x) = 1/\sqrt{1-x^2}$ is the Chebyshev weighting function. These integrals may be evaluated analytically. Following Gottlieb & Orszag (1977), we write

$$\frac{\mathrm{d}^q T_m}{\mathrm{d}x^q} = \sum_{k=0}^{\infty} a_k^{(q)}\, T_k(x), \tag{A 2}$$

where the coefficients are determined by the recurrence relation

$$c_{k-1} a_{k-1}^{(q)} - a_{k+1}^{(q)} = 2k a_k^{(q-1)} \qquad (k \geqslant 1), \tag{A 3}$$

with $c_0 = 2$, $c_k = 0$ if $k < 0$, and $c_k = 1$ if $k > 0$. By expanding $x^p T_n(x)$ in a series of Chebyshev polynomials, and making use of the orthogonality condition,

$$\int_{-1}^{1} w(x)\, T_n(x)\, T_k(x)\, \mathrm{d}x = \tfrac{1}{2}\pi\, c_k \delta_{nk}, \tag{A 4}$$

where δ_{nk} is the Kronecker delta, we derive

$$I = \frac{\pi}{2^{p+1}} \sum_{r=0}^{p} \binom{p}{r}\, a_{n+p-2r}^{(q)}\, c_{n+p-2r}, \tag{A 5}$$

which is valid for $n \geqslant p$, and any integer p. For the present purposes, it is sufficient to obtain a second formula, valid when $n < p \leqslant 5$. Writing

$$T_n(x) = \sum_{k=0}^{n} b_k^{(n)} x^k, \tag{A 6}$$

where the coefficients $b_k^{(n)}$ are known (e.g. Abramowitz & Stegun 1972, p. 795), and furthermore writing

$$x^{p+k} = \sum_{i=0}^{p+k} d_i^{(p,k)}\, T_i(x), \tag{A 7}$$

where the coefficients $d_i^{(p,k)}$ are also known (e.g. Abramowitz & Stegun 1972, p. 795), and applying the orthogonality condition (A 4), we find

$$I = \sum_{k=0}^{n} b_k^{(n)} \sum_{r=0}^{m-q} a_r^{(q)}\, Q_r^{(p,k)}, \tag{A 8}$$

where

$$Q_r^{(p,k)} = \begin{cases} \frac{1}{2}\pi c_r d_r^{(p,k)} & \text{if} \quad r \leqslant p+k, \\ 0 & \text{otherwise.} \end{cases} \tag{A 9}$$

Appendix B. Linear stability analysis for Stokes flow

In this Appendix, we present the linear stability analysis of core–annular flow in the presence of an insoluble surfactant, in the limit of vanishing Reynolds number where the flow is governed by the equations of Stokes flow. In the unperturbed configuration, the surfactant concentration is uniform, and the fluid motion is unidirectional and

parallel to the pipe wall, as discussed in § 2. The basic velocity profile is given in (2.5), and the pressure distribution state is given in (2.7). A normal-mode perturbation displaces the interface to a position given by the real or imaginary part of (3.1). The perturbation streamfunction, $\psi_j^{(1)}$, and vorticity, $\omega_j^{(1)}$, in either fluid satisfy

$$\mathscr{D}^2\psi_j^{(1)} = -\sigma\,\omega_j^{(1)}, \qquad \mathscr{D}^2\big(\sigma\,\omega_j^{(1)}\big) = 0, \tag{B 1}$$

where the operator $\mathscr{D}$ is defined in (3.5). Introducing the normal-mode forms (3.6), we find that the general solution to (B 1), is given by

$$\psi_j^{(1)} = \sigma\,[a_{1,j}I_1(k\sigma) + b_{1,j}K_1(k\sigma) + a_{2,j}\sigma\,I_0(k\sigma) + b_{2,j}\sigma\,K_0(k\sigma)]\,\exp(\mathrm{i}k[x-ct]), \tag{B 2}$$

where the I, K are modified Bessel functions (Goren 1962). Substituting the expression for the pressure given in (3.6) in the x-component of the Stokes equation and simplifying, we find

$$\mathrm{i}k\,q_j = \frac{1}{\sigma}\frac{\partial}{\partial\sigma}\big(D^2\psi_j^{(1)}\big), \tag{B 3}$$

so that

$$q_j(\hat{\sigma}) = -\frac{\mathrm{i}k^3}{\hat{\sigma}}\left(\frac{\mathrm{d}^3\phi_j}{\mathrm{d}\hat{\sigma}^3} - \frac{1}{\hat{\sigma}}\frac{\mathrm{d}^2\phi_j}{\mathrm{d}\hat{\sigma}^2} + \left(\frac{1}{\hat{\sigma}^2}-1\right)\frac{\mathrm{d}\phi_j}{\mathrm{d}\hat{\sigma}}\right). \tag{B 4}$$

Substituting the preceding expressions in the kinematic condition (3.10), we obtain

$$(c-u_I)A_1 = a_{21}\,a I_0(\hat{k}) + a_{11}\,I_1(\hat{k}), \tag{B 5}$$

where $\hat{k} = ka$.

Next, we use the linear constitutive equation for the surfactant concentration to write $\gamma_1 = -(Ma\gamma_0/\Gamma_0)\,\Gamma_1$, where Ma is the Marangoni number. Substituting the preceding expressions in (3.16) and simplifying, we obtain

$$a[I_0(\hat{k}) + \hat{k}I_1(\hat{k})]a_{21} + [\hat{k}I_0(\hat{k}) - I_1(\hat{k})]a_{11} - \frac{2\lambda u_I a^2}{(b^2-a^2)}A_1 = [a(c-u_I) + \mathrm{i}\hat{k}D_s]\frac{\Gamma_1}{\Gamma_0}. \tag{B 6}$$

Now, because ϕ_1/σ and ϕ_1'/σ must be bounded at $\sigma = 0$, we must have $b_{11} = b_{21} = 0$. To satisfy the no-slip and no-penetration condition at the wall, we require $\phi_2 = \phi_2' = 0$ at $\sigma = b$. Using the properties of the Bessel functions, we find

$$I_1(\hat{b})\,a_{12} + K_1(\hat{b})\,b_{12} + bI_0(\hat{b})\,a_{22} + bK_0(\hat{b})\,b_{22} = 0, \tag{B 7a}$$

$$kI_0(\hat{b})\,a_{12} - kK_0(\hat{b})\,b_{12} + [2I_0(\hat{b}) + \hat{b}I_1(\hat{b})]\,a_{22} + [2K_0(\hat{b}) - \hat{b}K_1(\hat{b})]\,b_{22} = 0, \tag{B 7b}$$

respectively, where $\hat{b} \equiv kb$. The velocity must be continuous across the interface. Upon linearization, we find

$$u_1^{(1)} = u_2^{(1)}, \qquad w_1^{(1)} + \eta\frac{\partial w_1^{(0)}}{\partial\sigma} = w_2^{(1)} + \eta\frac{\partial w_2^{(0)}}{\partial\sigma} \tag{B 8a, b}$$

at $\sigma = a$. Equation(B 8a) gives

$$(a_{11}-a_{12})\,I_1(\hat{k}) + (a_{21}-a_{22})\,aI_0(\hat{k}) - b_{22}\,aK_0(\hat{k}) - b_{12}\,K_1(\hat{k}) = 0, \tag{B 9}$$

and (B 8b) gives

$$\begin{aligned}(a_{11}-a_{12})\,kI_0(\hat{k}) + [\hat{k}I_1(\hat{k}) + 2\,I_0(\hat{k})](a_{21}-a_{22})\\ + [\hat{k}K_1(\hat{k}) - 2\,K_0(\hat{k})]b_{22} + kK_0(\hat{k})\,b_{12} = 2\frac{a}{(b^2-a^2)}\,u_I(\lambda-1)A_1.\end{aligned} \tag{B 10}$$

The linearized normal and shear stress balance at the interface are given in (3.12) and (3.14). Substituting the preceding expressions and simplifying, we obtain

$$2\mathrm{i}\mu_1\hat{k}[\hat{k}I_0(\hat{k}) - I_1(\hat{k})]\,(\lambda a_{12} - a_{11}) - 2\mathrm{i}\mu_2\hat{k}[\hat{k}K_0(\hat{k}) + K_1(\hat{k})]\,b_{12}$$
$$+ 2\,\mathrm{i}\mu_2\,a\hat{k}^2\,I_1(\hat{k})\,(\lambda a_{22} - a_{21}) - 2\,\mathrm{i}\mu_2\,a\hat{k}^2\,K_1(\hat{k})\,b_{22} = \gamma_0(1-\hat{k}^2)\,A_1 - a\gamma_1, \quad \text{(B 11)}$$

and

$$\mu_1\,kI_1(\hat{k})\,(\lambda a_{12} - a_{11}) + \mu_1[I_1(\hat{k}) + \hat{k}I_0(\hat{k})]\,(\lambda a_{22} - a_{21}) + \mu_2\,kK_1(\hat{k})\,b_{12}$$
$$+ \mu_2[\hat{k}K_0(\hat{k}) - K_1(\hat{k})]\,b_{22} = -\tfrac{1}{2}\mathrm{i}\,\gamma_1, \quad \text{(B 12)}$$

respectively. The linearized transport equation (B 6) can be used to eliminate γ_1 from (B 11) and (B 12).

Equations (B 5), (B 7), (B 9), (B 10), (B 11) and (B 12) are finally assembled in the linear system

$$\boldsymbol{M}\cdot\boldsymbol{w} = \boldsymbol{0}, \quad \text{(B 13)}$$

where $\boldsymbol{M}$ is a 7×7 complex coefficient matrix and $\boldsymbol{w} = [a_{11}, a_{21}, a_{12}, a_{22}, b_{12}, b_{22}, A_1]^T$ is the vector of unknowns. Setting the determinant of $\boldsymbol{M}$ to zero yields a quadratic equation for the complex phase velocity c, corresponding to two normal modes. In practice, we use the algebraic manipulation package Maple to derive the quadratic coefficients and compute the roots corresponding to a pair normal modes.

REFERENCES

Abramowitz, M. & Stegun, I. A. 1972 *Handbook of Mathematical Functions*. Dover.

Blyth, M. G. & Pozrikidis, C. 2004*a* Evolution equations for the surface concentration of an insoluble surfactant; stability of an elongating thread and a stretched interface. *Theor. Comput. Fluid Dyn.* **17**, 147–164.

Blyth, M. G. & Pozrikidis, C. 2004*b* Effect of surfactants on the stability of two-layer channel flow. *J. Fluid Mech.* **505**, 59–86.

Blyth, M. G. & Pozrikidis, C. 2004*c* Effect of inertia on the Marangoni instability of two-layer channel flow. Part II: Normal mode analysis. *J. Engng Maths* **50**, 329–341.

Carroll, B. & Lucassen, J. 1974 Effect of surface dynamics on the process of droplet formation from supported and free liquid cylinders. *J. Chem. Soc. Faraday Trans.* **70**, 1228–1239.

Cassidy, K. J., Halpern, D., Ressler, B. G. & Grotberg, J. B. 1999 Surfactant effects in model airway closure experiments. *J. Appl. Physiol.* **87**, 415–427.

Davey, A. & Drazin, P. G. 1969 The stability of Poiseuille flow in a pipe. *J. Fluid Mech.* **36**, 209–218.

Dongarra, J. J., Straughan, B. & Walker, D. W. 1996 Chebyshev tau–QZ algorithm methods for calculating spectra of hydrodynamic stability problems. *Appl. Num. Maths* **22**, 399–434.

Drazin, P. G. & Reid, W. H. 1981 *Hydrodynamic Stability*. Cambridge.

Frenkel, A. L. & D. Halpern, D. 2002 Stokes-flow instability due to interfacial surfactant. *Phys. Fluids* **14**, 45–48.

Georgiou, E., Maldarelli, C., Papageorgiou, D. T. & Rumschitzki, D. S. 1992 An asymptotic theory for the linear stability of a core–annular flow in the thin annular limit. *J. Fluid Mech.* **243**, 653–677.

Goren, S. L. 1962 The instability of an annular thread of fluid. *J. Fluid Mech.* **12**, 309–319.

Gottlieb, D. & Orszag, S. A. 1977 *Numerical Analysis of Spectral Methods*. SIAM.

Grotberg, J. B. & Jensen, O. E. 2004 Biofluid mechanics in flexible tubes. *Annu. Rev. Fluid Mech.* **36**, 121–147.

Halpern, D. & Frenkel, A. L. 2003 Destabilization of a creeping flow by interfacial surfactant: linear theory extended to all wavenumbers. *J. Fluid Mech.* **485**, 191–220.

Hickox, C. E. 1971 Instability due to viscosity and density stratification in axisymmetric pipe flow. *Phys. Fluids* **14**, 251–262.

Joseph, D. D., Bai, R., Chen, K. P. & Renardy, Y. Y. 1997 Core–annular flows. *Annu. Rev. Fluid Mech.* **29**, 65–90.

Joseph, D. D. & Renardy, Y. Y. 1993 *Fundamentals of Two-Fluid Dynamics, Part 1: Mathematical Theory and Applications, Part 2: Lubricated Transport, Drops and Miscible Liquids*. Springer.

Joseph, D. D., Renardy, M. & Renardy, Y. Y. 1984 Instability of the flow of two immiscible liquids with different viscosities in a pipe. *J. Fluid Mech.* **141**, 309–317.

Kas-Danouche, S., Papageorgiou, D. & Siegel, M. 2004 A mathematical model for core–annular flows with surfactants. *Divulgaciones Matemáticas* **12**(2), 117–138.

Kouris, C. & Tsamopoulos, J. 2001 Dynamics of axisymmetric core–annular flow in a straight tube. I. The more viscous fluid in the core, bamboo waves. *Phys. Fluids* **13**, 841–858.

Kouris, C. & Tsamopoulos, J. 2002 Dynamics of axisymmetric core–annular flow. II. The less viscous fluid in the core, saw tooth waves. *Phys. Fluids* **14**, 1011–1029.

Kwak, S. & Pozrikidis, C. 2001 Effect of surfactants on the instability of a liquid thread or annular layer. Part I: Quiescent fluids. *Intl J. Multiphase Flow* **27**, 1–37.

Li, J. & Renardy, Y. Y. 1999 Direct simulation of unsteady axisymmetric core–annular flow with high viscosity ratio. *J. Fluid Mech.* **391**, 123–149.

Li, X. & Pozrikidis, C. 1997 The effect of surfactants on drop deformation and on the rheology of dilute emulsions in Stokes flow. *J. Fluid Mech.* **341**, 165–194.

Orszag, S. A. 1971 Accurate solution of the Orr–Sommerfeld stability equation. *J. Fluid Mech.* **50**, 689–703.

Otis, D. R., Johnson, M., Pedley, T. J. & Kamm, R. D. 1993 Role of pulmonary surfactant in airway closure: a computational study. *J. Appl. Physiol.* **75**, 1323–1333.

Peskin, C. S. 2002 The immersed boundary method. *Acta Numerica* **11**, 479–517.

Pozrikidis, C. 1997 *Introduction to Theoretical and Computational Fluid Dynamics*. Oxford University Press, 675 pp.

Pozrikidis, C. 1998 *Numerical Computation in Science and Engineering*. Oxford University Press, 627 pp.

Pozrikidis, C. 2003 On the relationship between the pressure and the projection function for the numerical computation of incompressible flow. *Eur. J. Mech.* B /*Fluids* **22**, 105–121.

Pozrikidis, C. 2004*a* Instability of multi-layer channel and film flows. *Adv. Appl. Mech.* **40**, 179–239.

Pozrikidis, C. 2004*b* Effect of inertia on the Marangoni instability of two-layer channel flow. Part I: Numerical simulations. *J. Engng Maths* **50**, 311–327.

Preziosi, L., Chen, K. & Joseph, D. D. 1989 Lubricated pipelining: stability of core–annular flow. *J. Fluid Mech.* **201**, 323–356.

Renardy, Y. Y. 1997 Snakes and corkscrews in core–annular down-flow of two fluids. *J. Fluid Mech.* **340**, 297–317.

Russo, M. J. & Steen, P. H. 1989 Shear stabilization of the capillary breakup of a cylindrical interface. *Phys. Fluids* A **1**, 1926–1937.

Sheth, K. & Pozrikidis, C. 1995 Effects of inertia on the deformation of liquid drops in simple shear flow. *Comput. Fluids* **24**, 101–119.

Tryggvason, G., Bunner, B., Esmaeeli, A., Juric, D., Al-Rawahi, N., Tauber, W., Han, J., Nas, S. & Jan, Y.-J. 2001 A front-tracking method for the computations of multiphase flow. *J. Comput. Phys.* **169**, 708–759.

Yon, S. & Pozrikidis, C. 1998 A finite-volume/boundary-element method for flow past interfaces in the presence of surfactants, with application to shear flow past a viscous drop. *Comput. Fluids* **27**, 879–902.

Wei, H.-H. 2005 Marangoni destabilization on a core–annular film flow due to the presence of surfactant. *Phys. Fluids* **17**, 027101.

Wei, H.-H., Halpern, D. & Grotberg, J. B. 2005 Linear stability of a surfactant-laden annular film in a time-periodic pressure-driven flow through a capillary. *J. Colloid Innterface Sci.* **285**, 769–780.

Wei, H.-H. & Rumschitzki, D. S. 2002*a* The linear stability of a core–annular flow in an asymptotically corrugated tube. *J. Fluid Mech.* **466**, 113–147.

Wei, H.-H. & Rumschitzki, D. S. 2002*b* The weakly nonlinear interfacial stability of a core–annular flow in a corrugated tube. *J. Fluid Mech.* **466**, 149–177.

Wei, H.-H. & Rumschitzki, D. S. 2005 The effects of insoluble surfactants on the linear stability of a core–annular flow. *J Fluid Mech.* **541**, 115–142.